Mon. Not. R. Astron. Soc. **000**, 1–18 (2011) Printed 3 December 2013 (MN LATEX style file v2.2)

Spatially Resolved Velocity Maps of Halo Gas Around Two Intermediate-redshift Galaxies⋆

Hsiao-Wen Chen[1]†, Jean-René Gauthier[2], Keren Sharon[3], Sean D. Johnson[1], Preethi Nair[4], Cameron J. Liang[1]

[1]*Department of Astronomy & Astrophysics, and Kavli Institute for Cosmological Physics, University of Chicago, Chicago, IL 60637, USA*
[2]*Cahill Center for Astronomy and Astrophysics, California Institute of Technology, Pasadena, CA 91125, USA*
[3]*Department of Astronomy, University of Michigan, 500 Church Street, Ann Arbor, MI 48109, USA*
[4]*Space Telescope Science Institute, Baltimore, MD 21218, USA*

3 December 2013

ABSTRACT

Absorption-line spectroscopy of multiply-lensed QSOs near a known foreground galaxy provides a unique opportunity to go beyond the traditional one-dimensional application of QSO probes and establish a crude three-dimensional (3D) map of halo gas around the galaxy that records the line-of-sight velocity field at different locations in the gaseous halo. Two intermediate-redshift galaxies are targeted in the field around the quadruply-lensed QSO HE 0435−1223 at redshift $z = 1.689$, and absorption spectroscopy along each of the lensed QSOs is carried out in the vicinities of these galaxies. One galaxy is a typical, star-forming L_* galaxy at $z = 0.4188$ and projected distance of $\rho = 50$ kpc from the lensing galaxy. The other is a super-L_* barred spiral at $z = 0.7818$ and $\rho = 33$ kpc. Combining known orientations of the quadruply-lensed QSO to the two foreground galaxies with the observed Mg II $\lambda\lambda$ 2796,2803 absorption profiles along individual QSO sightlines has for the first time led to spatially resolved kinematics of tenuous halo gas on scales of $5 - 10$ kpc at $z > 0.2$. A Mg II absorber is detected in every sightline observed through the halos of the two galaxies, and the recorded absorber strength is typical of what is seen in previous close QSO–galaxy pair studies. While the multi-sightline study confirms the unity covering fraction of Mg II absorbing gas at $\rho < 50$ kpc from star-forming disks, the galaxies also present two contrasting examples of complex halo gas kinematics. Different models, including a rotating disk, collimated outflows, and gaseous streams from either accretion or tidal/ram-pressure stripping, are considered for comparisons with the absorption-line observations, and infalling streams/stripped gas of width $\gtrsim 10$ kpc are found to best describe the observed gas kinematics across multiple sightlines. In addition, the observed velocity dispersion between different sightlines offers a crude estimate of turbulence in the Mg II absorbing halo gas. The observations presented here demonstrate that multiple-QSO probes enable studies of spatially resolved gas kinematics around distant galaxies, which provide key insights into the physical nature of circumgalactic gas beyond the nearby universe.

Key words: galaxies:halos – galaxies:intergalactic medium – quasars:absorption lines – galaxies:kinematics and dynamics

1 INTRODUCTION

A key element in theoretical studies of galaxy formation and evolution is an accurate characterization of gas infall and outflows around star-forming regions, two competing processes that regulate star formation over cosmic time. Capturing these processes in observations is therefore of great

⋆ Based on data gathered with the 6.5 m Magellan Telescopes located at Las Campanas Observatory, and the NASA/ESA Hubble Space Telescope operated by the Space Telescope Science Institute and the Association of Universities for Research in Astronomy, Inc., under NASA contract NAS 5-26555

† E-mail:hchen@oddjob.uchicago.edu

interest and importance in validating our view of how galaxies grow. Since the pioneering work of Boksenberg & Sargent (1978), Boksenberg et al. (1980), and Bergeron (1986), absorption spectroscopy of distant QSOs has been utilized as an effective means of probing tenuous gas around galaxies. For every projected galaxy and QSO pair, the background QSO serves as a single pencil beam to explore the line-of-sight gas distribution through the galactic halo at the projected distance where the QSO appears.

While QSO absorption spectroscopy offers unparalleled sensitivities for uncovering low-density gas, a single QSO spectrum does not yield a two-dimensional map of halo gas around individual galaxies like conventional 21 cm observations (e.g. Chynoweth et al. 2008). Studies of halo gas around distant galaxies have therefore relied on a statistical approach to characterize the spatial distribution of tenuous gas in galactic halos (e.g. Lanzetta & Bowen 1990) and to estimate a mean value of gas covering fraction (e.g. Lanzetta et al. 1995; Chen et al. 2010a; Tumlinson et al. 2011) over an ensemble of intervening galaxies. However, details regarding the spatial variation of gas density and kinematics remain unknown for individual halos. Knowing the kinematics of halo gas revealed in absorption-line surveys bears significantly on all effort to characterize gas infall and outflows around star-forming galaxies using absorption spectroscopy (e.g. Faucher-Giguère & Kereš 2011).

Recent galaxy survey data have revealed the ubiquitous presence of outflows in star-forming galaxies at $z > 0.7$, through observations of blue-shifted Mg II $\lambda\lambda$ 2796,2803 self-absorption against the UV light from star-forming regions (e.g. Weiner et al. 2009; Rubin et al. 2010; Bordoloi et al. 2013). Although the distance of the outflowing material is unknown in these observations (but see Rubin et al. 2011 and Martin et al. 2012 for two cases that exhibit outflowing gas in emission out to ~ 10 kpc), such finding has triggered several follow-up studies that attribute the majority of metal-line absorbers (such as Mg II, C IV, and O VI) uncovered along random sightlines to those high-speed outflows revealed through self-absorption of UV light (e.g. Steidel et al. 2010; Chelouche & Bowen 2010; Nestor et al. 2011; Tumlinson et al. 2011; Werk et al. 2013). Such interpretation naturally implies a minimal presence of gas accretion around star-forming galaxies.

An additional empirical finding that supports the notion of a non-negligible fraction of metal-line absorbers originating in starburst driven outflows is the enhanced Mg II absorption near the minor axes and within 50 projected kpc of disk galaxies at $z \sim 0.7$ by Bordoloi et al. (2011). This finding has been followed by reports of a possible bimodal azimuthal dependence of Mg II absorbers (e.g. Bouché et al. 2012; Kacprzak et al. 2012), attributing metal-line absorbers observed near minor axes to outflowing gas and those observed near major axes to infalling gas. A bimodal distribution in the disk orientation of a Mg II-selected galaxy sample suggests that both gas infall and outflows contribute comparably to the absorber population. It also suggests that the physical origin of an absorber can be determined if the disk orientation is known. However, the velocity field of outflows/accretion is not known and such report has also raised new questions.

For example, a natural expectation for absorption lines produced in outflows is that the observed velocity profile depends on the inclination of the star-forming disk, with the largest velocity spread expected when looking directly into a face-on star-forming disk (e.g. Gauthier & Chen 2012). While such inclination-dependent absorption width is clearly seen in the self-absorption of galaxy UV light (e.g. Kornei et al. 2012; Bordoloi et al. 2012), it appears to be weak or absent among random absorbers found in transverse direction from star-forming galaxies (e.g. Bordoloi et al. 2011; Bouché et al. 2012). The lack of correlation between absorber width and disk inclination appears to be discrepant from the expectations of an outflow origin. In addition, galactic-scale outflows in local starbursts are observed to follow the path of least resistance along the polar axis (e.g. Heckman et al. 1990). If this feature also applies to distant star-forming galaxies, then known disk orientation and inclination allow us to deproject the observed line-of-sight velocity distribution along the polar axis and examine the energetics required to power the outflows. Gauthier & Chen (2012) showed that if the Mg II absorbers observed at $\rho > 7$ kpc from star-forming galaxies originate in outflows, then either the outflows are decelerating (inconsistent with the interpretation of blue-shifted absorption tails by Martin & Bouché 2009 and Steidel et al. 2010) or there needs to be additional kinetic energy input at > 10 kpc beyond the disk plane. Finally, Chen (2012) showed that both the spatial extent and mean absorption equivalent width of halo gas around galaxies of comparable mass have changed little since $z \approx 2.2$, despite the observations that individual galaxies at $z \approx 2$ on average were forming stars at > 20 times faster rate than low-redshift galaxies (Wuyts et al. 2011). The constant spatial profile in absorption around galaxies of disparate star formation properties is difficult to reconcile, if these absorbers originate primarily in starburst driven outflows. Consequently, the origin of halo gas revealed in absorption spectroscopy remains an open question and to fully understand the origin and growth of gaseous halos around galaxies requires new observations.

To go beyond the traditional one-dimensional application of QSO probes, we have targeted two intermediate-redshift galaxies in the field around the quadruply-lensed QSO HE 0435−1223 at $z = 1.689$ (Wisotzki et al. 2002) and searched for absorption features in the spectra of individual lensed QSO images that are associated with the galaxies. The four QSO images are separated by $\approx 1.6'' - 2.5''$ (Figure 1) and serve as a natural integral field unit for mapping the kinematics of halo gas around individual galaxies in the foreground. A fundamental difference between our study and previous absorption-line analyses toward lensed or binary QSOs (e.g. Rauch et al. 1999, 2001a,b, 2002; Martin et al. 2010) is in the prior knowledge of the locations of the associated galaxies. Absorption-line spectroscopy of multiply-lensed QSOs near a known foreground galaxy allows us to establish a crude three-dimensional (3D) map of halo gas around the galaxy that records the line-of-sight velocity field along with the two-dimensional (2D) distribution of absorption strength. Combining the absorption profiles revealed along multiple sightlines with known orientation of the star-forming disk with respect to individual sightlines allows us for the first time to resolve the kinematics of tenuous halo gas on scales of $5 - 10$ kpc for galaxies at $z > 0.2$ (cf. Verheijen et al. 2007), and offers a unique opportunity

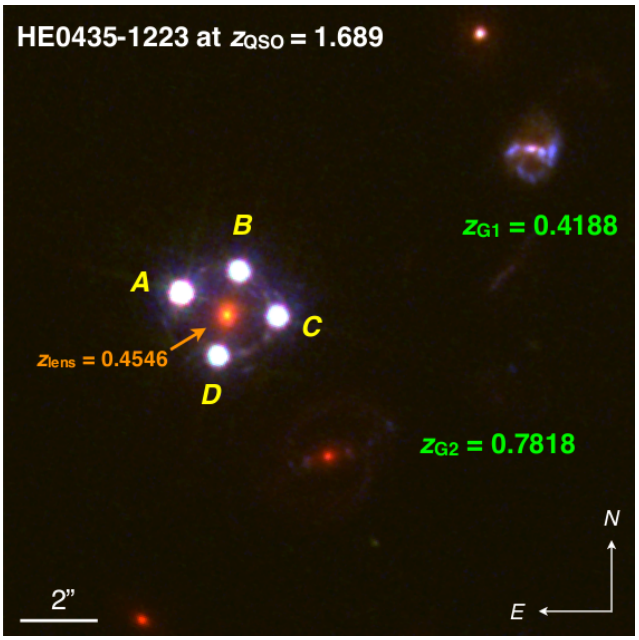

Figure 1. Optical composite image of the field surrounding HE0435−1223 made using the HST/WFC3 UVIS channel and the F275W filter, and ACS WFC and the F555W and F814W filters. The four lensed images ($ABCD$) of the background QSO at $z = 1.689$ are well resolved from the lens at $z_{\rm lens} = 0.4546$ with a maximum angular separation of $\overline{AC} = 2.5''$. Galaxies, $G1$ and $G2$, are spectroscopically identified at $z = 0.4188$ and $z = 0.7818$, respectively (see § 3 for discussion).

to begin to constrain models for inflows and galactic-scale outflows.

In the field around HE 0435−1223, we have identified two galaxies in close projected distances from the lensed QSOs (at angular separations $\theta < 10''$). As demonstrated in the following sections, one is a typical blue star-forming galaxy at redshift $z = 0.4188$ and the other is a massive quiescent star-forming barred spiral at $z = 0.7818$. High-quality images of the field are available in the *Hubble Space Telescope* (HST) data archive, allowing us to obtain accurate measurements of the orientation of the star-forming disks. Here we present spatially resolved velocity maps of halo gas around these two intermediate-redshift galaxies based on a joint analysis of absorption-line observations and relative alignments between the star-forming disks and each of the four QSO sightlines.

This paper is organized as follows. In Section 2, we describe the observations and data reduction. In Section 3, we present the observed and derived photometric and spectroscopic properties of two galaxies in the foreground of the lensed QSO. In Section 4, we take into account known morphologies of the galaxies and present the velocity maps of their gaseous halos. We compare the observations with predictions based on different models and discuss the implications of our results in Section 5, and summarize the results of our study in Section 6. We adopt a ΛCDM cosmology, $\Omega_{\rm M} = 0.3$ and $\Omega_\Lambda = 0.7$, with a Hubble constant $H_0 = 70$ km s^{-1} Mpc^{-1} throughout the paper.

2 OBSERVATIONS AND DATA REDUCTION

To spatially resolve the velocity field of halo gas around galaxies, both high spatial resolution images of the galaxies and high spectral resolution absorption spectra of background QSOs are needed. The high spatial resolution images of the galaxies allow us to determine the orientation and inclination of the star-forming disks relative to the lines of sight to the background QSOs. The high spectral resolution absorption spectra allow us to resolve individual absorbing components, thereby characterizing gas flows in galactic halos. In addition, moderate-resolution spectra of the galaxies enable both precise measurements of their systemic redshifts and accurate measurements of the gas-phase metallicity in the star-forming ISM. Here we describe available imaging and spectroscopic data for the field around HE 0435−1223.

2.1 Imaging Observations

Optical imaging observations of the field around HE 0435−1223 were performed with the HST Advanced Camera for Surveys (ACS) using the F555W and F814W filters (PID 9744; PI: C. Kochanek). Additional imaging observations of this field were performed with the HST Wide Field Camera 3 (WFC3) using the UVIS channel and the F275W filter (PID 11732; PI: C. Kochanek). The imaging data were retrieved from the HST data archive and processed using the standard reduction pipeline. We registered these frames to a common origin using stars in the field. A color composite image of the field around the lens is presented in Figure 1. The mean FWHM of the point spread function for all three filters is approximately $0.1''$. In the ACS images, the four lensed images ($ABCD$) of the background QSO at $z = 1.689$ are well resolved from the lens at $z_{\rm lens} = 0.4546$ with a maximum angular separation of $\overline{AC} = 2.5''$ between images A and C.

2.2 Galaxy Spectroscopy

We have obtained optical spectra of two spiral galaxies, $G1$ and $G2$, at angular separations $\theta_{\rm lens} < 10''$ from the lens (Figure 1). The galaxies were selected based on their proximity to the line of sight toward the quad lens. $G1$ at $\theta_{\rm lens} = 8.9''$ was targeted spectroscopically by Morgan et al. (2005), who reported a redshift measurement of $z = 0.4191 \pm 0.0002$. $G2$ at $\theta_{\rm lens} = 4.4''$ was considered a possible member associated with the gravitational lens at $z_{\rm lens} = 0.45$, but detailed lens models from previous studies by Wisotzki et al. (2003) and Morgan et al. (2005) showed that this galaxy is likely located at a cosmologically distinct redshift from the lens. We targeted both galaxies for spectroscopy. The observations were carried out using MagE (Marshall et al. 2008) on the Magellan Clay Telescope at the Las Campanas Observatory.

MagE is a high-throughput echellette spectrograph that offers a contiguous spectral coverage from $\lambda = 3100$ Å through 1 μm. We used a $1''$ slit and 2×1 binning during readout, which yielded a spectral resolution of FWHM $\approx$ 150 km s^{-1}. The observations of each galaxy were carried out on the night of 15 December 2012 in a sequence of two exposures of duration 900 s to 1800 s each. The slit was

aligned along the optimal parallactic angle for the duration of the observations. The mean seeing condition over the period of integration was $0.8''$. The galaxy data were processed and reduced using the data reduction software described in Chen et al. (2010a). In summary, wavelengths were calibrated using a ThAr frame obtained immediately after each exposure and subsequently corrected to vacuum and heliocentric wavelengths. Cross-correlating the observed sky spectrum with the sky emission atlas published by Hanuschik (2003) confirmed that the wavelength calibration was accurate to ≈ 7 km s^{-1}. Relative flux calibration was performed to correct for the response function of individual echellette orders, using a sensitivity function derived from earlier observations of the flux standard EG274. Individual flux-calibrated orders were coadded to form a single spectrum.

2.3 QSO Absorption Spectroscopy

Echellette spectroscopic observations of the lensed QSOs were obtained using MagE on 31 August 2011. The observations were carried out using a $1''$ slit and 1×1 binning during readout, which yielded a spectral resolution of FWHM ≈ 70 km s^{-1}. The mean seeing condition over the period of integration was $\approx 0.7'' - 0.8''$. The total exposure time accumulated for each lensed QSO ranged from 3300 seconds for images A and C to 3600 seconds for image D. The QSO spectra were processed and reduced using the same customized reduction pipeline described in § 2.2. Individual echellette orders were continuum normalized and coadded to form a single spectrum that covers a spectral range from $\lambda = 3050$ Å to $\lambda = 1\,\mu$m. The continuum was determined using a low-order polynomial fit to spectral regions that are free of strong absorption features. The continuum-normalized spectra have $S/N \gtrsim 10 - 20$ per resolution element at $\lambda \gtrsim 3800$ Å.

To resolve gas kinematics in galactic halos, higher resolution absorption spectra are necessary. We have therefore attempted echelle spectroscopy for the lensed QSOs, using the MIKE echelle spectrograph (Bernstein et al. 2003) on the Magellan Clay telescope. MIKE delivers an unbinned pixel resolution of $0.12''$ along the spatial direction and ≈ 0.02 Å along the spectral direction in the blue arm that covers a wavelength range from $\lambda = 3200$ Å through $\lambda = 5000$ Å. The observations were carried out on the nights of 15 and 16 of December 2012. The mean seeing condition over this period was $0.7''$. Because the lensed QSOs are faint with $g_A = 19.0$, $g_B = 19.5$, $g_C = 19.6$, and $g_D = 19.6$ mag (Wisotzki et al. 2002), we experimented with two sets of heavy binning 3×3 and 2×4 during readout in order to achieve sufficient signal ($S/N \approx 10$ per resolution element) in a reasonable amount of exposure time. While the instrument line spread function is slightly under-sampled with the adopted binning, the observations still allow us to resolve velocity profiles on scales of ~ 10 km s^{-1}.

We succeeded in observing three (ABC) of the four lensed QSO images using MIKE. QSO image B was observed on the first night. The observations consist of 3×3600 s exposures. We used a $0.7''$ slit and 3×3 binning during readout, which yielded a spectral resolution of FWHM ≈ 9 km s^{-1} at $\lambda = 4000$ Å. However, it quickly became clear that the heavy binning along the spatial direction makes an accurate sky subtraction challenging with image A at $\approx 1.6''$ away. We therefore observed A and C on the second night, using a $0.7''$ slit and 2×4 (spatial $\times$ spectral) binning during readout. The observations include a total exposure time of 5200 s and 6600 s for A and C, respectively.

The data were processed and reduced using a customized reduction pipeline developed by G. Becker and kindly offered to us by the author. In summary, individual spectral images were first bias-subtracted and corrected for pixel-to-pixel variation using twilight flats obtained through a diffuser. Next, a 2D wavelength map, corrected to vacuum and heliocentric wavelengths, was produced using a ThAr frame obtained immediately after each exposure. Object spectra were then optimally extracted using a Gaussian profile that matches the width of object profile along the cross-dispersion direction in each order. Neighboring objects (other lensed images in the case presented here) that moved into the slit during individual exposures were masked during spectrum extraction. Next, flux calibration was performed using a sensitivity function derived from observations of the flux standard Feige 110, and individual flux calibrated echelle orders were coadded to form a single spectrum. Finally, these order-combined individual exposures were continuum normalized and stacked to form one final combined spectrum per QSO using an optimal weighting routine. The continuum was determined using a low-order polynomial fit to spectral regions that are free of strong absorption features.

3 ANALYSIS OF GALAXY PROPERTIES

The HST images described in § 2.1 show that while the two galaxies at $\theta_{\rm lens} < 10''$ from the lens (Figure 1) can be generally characterized as nearly face-on barred spirals, they display distinct colors and resolved morphologies. Specifically, $G1$ at $z = 0.4188$ shows enhanced star-forming regions with luminous UV radiation across the central bar and along the spiral arms, and $G2$ at $z = 0.7818$ shows a well-developed central bar and two spiral arms that are dominated by older stellar population with some trace of on-going star formation at the ends of the bar and the spiral arms (as revealed by faint UV emission; see also Figure 7).

We measure the inclination angle (i_0) of each galaxy based on the ratio of the observed spatial extent along the major and minor axes, and find that $i_0 = 40^\circ$ for $G1$ and $i_0 = 25^\circ$ for $G2$. Uncertainties in the inclination angle are roughly $\pm3^\circ$. We also measure the position angle of the major axis on the sky and find P.A. $= 173^\circ$ measured north through east for $G1$ and P.A. $= 13^\circ$ for $G2$. Uncertainties in the position angle are roughly $\pm5^\circ$. Here we summarize photometric and spectroscopic properties of these two galaxies.

3.1 $G1$ at $z = 0.4188$

We first note that Morgan et al. (2005) analyzed the ACS F555W and F814W images and measured $4''$-diameter aperture photometry for this galaxy. These authors reported $m_{\rm F555W} = 21.18 \pm 0.02$ and $m_{\rm F814W} = 21.16 \pm 0.01$ in the STmag system (e.g. Koorneef et al. 1986). In addition, they obtained an optical spectrum of the galaxy and measured a mean redshift $z = 0.4191 \pm 0.0002$ based on observations

Table 1. Summary of Galaxy Properties

	$z_{\rm gal}$	$\theta_{\rm lens}$ ($''$)	ρ (kpc)	i_0 ($^\circ$)	P.A.^{a} ($^\circ$)	AB(F275W, F555W, F814W)^b (mag)	M_B (mag)	12 + log(O/H)	EW$_{\rm H\alpha}$ (Å)	SFR ($M_\odot$/yr)	M_* ($M_\odot$)
$G1$	0.4188	8.9	49	40	173	$(23.39 \pm 0.02, 21.16 \pm 0.01, 20.39 \pm 0.01)$	-20.5	8.32 ± 0.07	80 ± 5	4.3	$(2-3) \times 10^{10}$
$G2$	0.7818	4.4	33	25	13	$(24.50 \pm 0.04, 22.35 \pm 0.02, 20.79 \pm 0.01)$	-22.0	...	...	> 0.8	$\approx 8 \times 10^{10}$

^{a}Position angle of the inclined disk measured north through east.
^{b}Aperture photometry measured in a $4''$ diameter aperture centered at the galaxy.

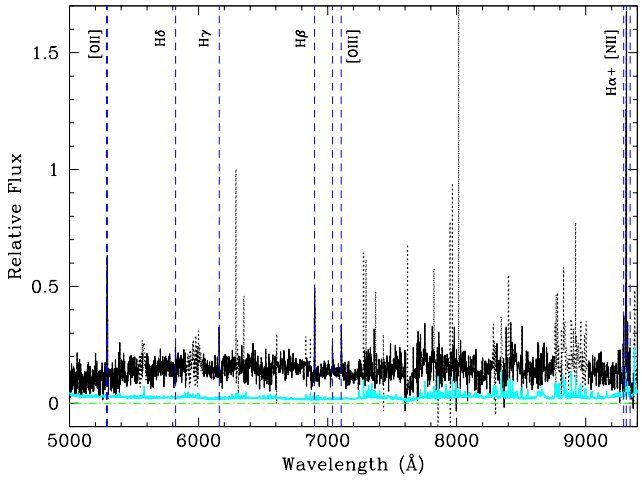

Figure 2. Optical spectrum of $G1$ obtained using MagE on the Magellan Clay Telescope. The data reveal numerous emission features (marked by long dashed lines) with a mean redshift at $z = 0.4188 \pm 0.0001$. The corresponding 1-σ error spectrum is shown in cyan at the bottom above the zero flux level (dash-dotted line). Contaminating sky residuals are dotted out for clarification.

of [O II], Hβ, and [O III]. Furthermore, these authors also noted the presence of a second galaxy at $z = 0.4189$ at 3.5 times angular distance away, $\theta_{\rm lens} = 31.4''$ (G22 in their paper), suggesting that $G1$ may be associated with a galaxy group.

Our MagE observations of $G1$ confirm that the galaxy spectrum is dominated by a blue continuum and strong emission line features (Figure 2). In addition to [O II], Hβ (which occurs in the terrestrial atmospheric B band absorption), and [O III], we also detect [N II], Hα, and higher-order Balmer emission lines. A cross-correlation analysis with a linear combination of SDSS eigen spectra of galaxies returns a best-fit redshift and redshift uncertainty of $z = 0.4188 \pm 0.0001$. At this redshift, the projected distance between $G1$ and the lens is $\rho = 49$ kpc.

We determine the interstellar oxygen abundance of $G1$ using the semi-empirical correlation between $12 + \log({\rm O/H})$ and $N2 \equiv \log[{\rm N\,II}]/{\rm H}\alpha$ from Pettini & Pagel (2004). We adopt the $N2$ index for the interstellar oxygen abundance measurement of $G1$, because it is based on two closely located lines ([N II] λ6853 and Hα) and not sensitive to uncertainties in flux calibration and/or differential dust extinction. Based on the observed [N II] and Hα line ratio, we derive $12 + \log({\rm O/H}) = 8.32 \pm 0.07$ for the gas phase abundance in the ISM of $G1$.

To determine the intrinsic luminosity, color, stellar mass, and star formation rate (SFR) of the galaxy, we also measure aperture photometry of galaxy $G1$ in the archival optical and UV images obtained using HST ACS and WFC3. Within a $4''$ diameter aperture, we measure $AB({\rm F275W}) = 23.39 \pm 0.02$, $AB({\rm F555W}) = 21.16 \pm 0.01$, $AB({\rm F814W}) = 20.39 \pm 0.01$. At $z = 0.4188$, the observed apparent magnitudes lead to rest-frame absolute magnitudes of $M_B = -20.5$ in the B band and $M_R = -21.3$ in the R band, and $g - r$ color of $g - r = 0.4$ mag for the galaxy.

Adopting the color-based stellar mass-to-light ratio M_*/L from Bell et al. (2003) for different stellar initial mass functions, we estimate a total stellar mass of $M_* \approx (2-3) \times 10^{10}\,{\rm M}_\odot$ for $G1$. Adopting the stellar mass to halo mass relation of Behroozi et al. (2010), we further estimate the dark matter halo mass of $G1$ to be $M_h \sim 10^{12}\,{\rm M}_\odot$. Finally, we estimate the on-going SFR based on the observed Hα equilvalent width (EW$_{\rm H\alpha}$) and rest-frame R-band magnitdue. We measure EW$_{\rm H\alpha} = -80 \pm 5$ Å and infer a total Hα flux of $f_{\rm H\alpha} = 8 \times 10^{41}$ erg s^{-1} under the assumption that EW$_{\rm H\alpha}$ is roughly constant across the disk. Adopting the star formation rate calibration of Kennicutt & Evans (2012), we estimate an unobscured SFR of $\approx 4.3\,{\rm M}_\odot\,{\rm yr}^{-1}$ for $G1$ which is roughly six times higher than the SFR inferred from the observed UV flux in the F275W band. The difference between Hα and UV inferred SFR can be attributed to either dust extinction or spatial inhomogeneities in EW$_{\rm H\alpha}$. We cannot constrain the dust content based on the observed flux ration between Hα and Hβ lines, because Hβ falls in the atmosphere B-band absorption.

A summary of the optical properties of $G1$ is presented in the first row of Table 1. We conclude that $G1$ at $z = 0.4188$ is an L_* galaxy with photometric properties consistent with typical blue star-forming galaxies at $z \sim 0.4$ (e.g. Noeske et al. 2007; Zhu et al. 2011).

3.2 $G2$ at $z = 0.7818$

Optical photometry of this galaxy has also been reported by Morgan et al. (2005), who measured $m_{\rm F555W} = 22.25 \pm 0.04$ and $m_{\rm F814W} = 21.26 \pm 0.01$ in the STmag system over a $4''$-diameter aperture. However, no spectroscopic observations have been made by this team. It is possible that $G2$ and the lens are correlated, because of a small angular distance ($\theta_{\rm lens} = 4.4''$, corresponding to $\rho = 25$ kpc at $z = 0.45$) between the two galaxies. But as noted earlier by Wisotzki et al. (2003) and Morgan et al. (2005), detailed lens models have shown that $G2$ is more likely located at a cosmologically distinct redshift from the lens.

Our MagE observations of $G2$ revealed a faint emission line at 6644 Å, along with absorption features that are consistent with [O II] and Ca II H&K absorption doublet at $z = 0.7818$. Figure 3 shows both the extracted one-dimensional

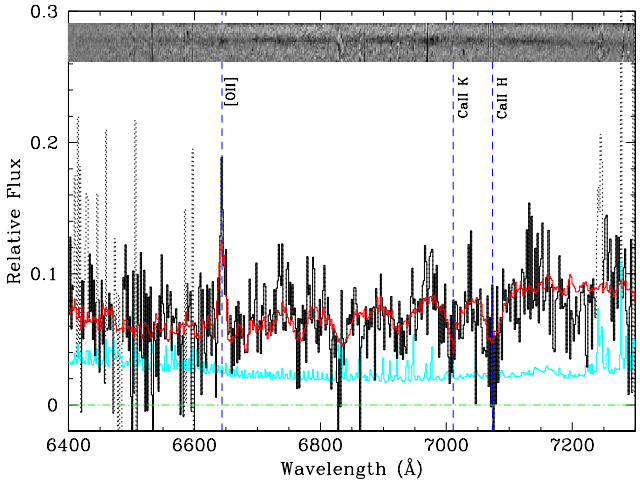

Figure 3. Optical spectrum of $G2$ obtained using MagE on the Magellan Clay Telescope. The corresponding 1-σ error spectrum is shown in cyan at the bottom above the zero flux level (dash-dotted line), while a rectified two-dimensional spectral image is presented at the top. Contaminating sky residuals are dotted out for clarification. We identify a faint emission line at 6644 Å, along with absorption features that are consistent with [O II] and Ca II H&K absorption doublet at $z = 0.7818$. We measure the redshift using a cross-correlation analysis with a linear combination of SDSS eigen spectra of galaxies. The best-fit model template is shown as the red spectrum, which also displays matched absorption features due to the Balmer series.

spectrum and the corresponding two-dimensional spectral image. At this redshift, Hβ and [O III] are covered by the MagE data but occur in the forest of OH sky lines. We therefore cannot robustly determine the presence/absence of Hβ and [O III] lines. A cross-correlation analysis with a linear combination of SDSS eigen spectra of galaxies returns a best-fit redshift and redshift uncertainty of $z = 0.7818 \pm 0.0004$. We present the best-fit model spectrum in red in Figure 3. Comparing the observed spectrum and best-fit model also reveals the presence of Balmer absorption series, suggesting a post-starburst nature of the galaxy.

We have also measured aperture photometry of galaxy $G2$ in the archival optical and UV images obtained using HST ACS and WFC3. Within a 4″ diameter aperture, we measure $AB(\mathrm{F275W}) = 24.50 \pm 0.04$, $AB(\mathrm{F555W}) = 22.35 \pm 0.02$, $AB(\mathrm{F814W}) = 20.79 \pm 0.01$. At $z = 0.7818$, the observed F814W band corresponds well with rest-frame B band. The observed F814W magnitude therefore translates to a rest-frame B-band absolute magnitude of $M_B = -22.0$ for $G2$, which is roughly $1.7\,L_*$ (Faber et al. 2007).

At $z = 0.78$, the rest-frame R band is redshifted into the observed J band. Without near-infrared photometry, we cannot accurately determine the total stellar mass of $G2$. While the apparent red color of $G2$ in Figure 1 indicate little on-going star formation, an accurate estimate of the total stellar would require rest-frame optical and near-infrared colors. Adopting the same mass-to-light ratio from $G1$ leads to $M_* \approx 8 \times 10^{10}\,\mathrm{M}_\odot$ and $M_h \sim 5 \times 10^{12}\,\mathrm{M}_\odot$ for $G2$. Finally, we constrain the on-going SFR based on the observed UV flux in the F275W band and derive an unobscured SFR of $> 0.8\ \mathrm{M}_\odot\,\mathrm{yr}^{-1}$ for $G2$.

A summary of the optical properties of $G2$ is presented in the second row of Table 1. We conclude that $G2$ at $z = 0.7818$ is a massive, super-L_* galaxy with spectroscopic properties similiar to quiescent star-forming galaxies at $z = 0.5 - 1$ (e.g. Poggianti et al. 2009).

4 VELOCITY MAPS OF GASEOUS HALOS

The available HST images have yielded important constraints for both the photometric and morphological properties of galaxies $G1$ and $G2$. The next step is to analyze the absorption profiles revealed along multiple sightlines, in order to establish a spatially resolved velocity map of absorbing clouds in the galactic halo.

The absorption-line analysis is, however, complicated due to a mixed spectral quality in the available data. As described in § 2.3, MIKE echelle spectroscopy was carried out for QSO sightlines A, B, and C, while MagE echellette observations were carried out for QSO sightlines A, C, and D during two different observing periods. The native spectral resolutions offered by MIKE and MagE are ≈ 10 and ≈ 70 km s^{-1}, respectively. In addition, because the QSO images are fainter than the nominal source brightness for attempting MIKE spectroscopy, we adopted heavy binning during readout to increase the observation efficiency. As a result, we are able to separate individual absorbing components separated by $\gtrsim 10$ km s^{-1} in the MIKE spectra, but we are unable to resolve individual resolution elements. For absorption spectra obtained with MagE, we cannot resolve features on scales < 70 km s^{-1}. The expectation is that while fluctuations on small velocity scales along a single line of sight may be lost due to heavy binning or low spectral resolution, large-scale velocity gradient across different lines of sight can still be resolved.

In this section, we first describe the procedures developed for analyzing the under-sampled absorption spectra. The results from individual sightlines are then combined to establish a crude 3D velocity map for the gaseous halos around $G1$ and $G2$, which are described in the subsequent sections.

4.1 Analysis of Absorption Profiles

A Mg II absorber is detected in every sightline through the halo of each of the two galaxies in our study. The absorber strength observed in these galaxies is typical of what is seen in previous close QSO–galaxy pair studies (e.g. Chen et al. 2010a,b). We focus our analysis on the observed Mg II absorption doublet, because these are the strongest transitions that can be observed in the optical echelle data and because in nearly all four sightlines these are the only transitions that are detected at $> 10\,\sigma$ level of significance. Given that only Mg II absorption is observed, we cannot obtain direct constraints for the physical properties of the gas. In the following analysis, we infer a mean gas metallicity based on the empirical metallicity–$W_r(2796)$ relation of Murphy et al. (2007; see also Ledoux et al. 2006), and assume an ionization fraction of $f_{\mathrm{Mg}^+} = 0.1$ based on a simple ionization model presented in Chen & Tinker (2008).

For $G1$, we have MIKE spectra available for sightlines

A, B, and C and MagE spectra available for D for a complete four-point mapping of its gaseous halo as offered by the quad-lens system. For $G2$, however, the associated Mg II absorption doublet occur near the cross-over wavelength of the dichroic in MIKE, where the signal-to-noise (S/N) of the data is particularly poor. Consequently, only MagE spectra of A, C, and D are available for mapping the gaseous halo of $G2$.

To account for the mixed spectral quality and derive a robust velocity map, we develop custom computer programs for analyzing the observed absorption profiles. The primary goal of our analysis is to obtain an accurate map of the velocity field across different sightlines.

We first characterize the observed absorption along each sightline as due to discrete clouds. Under this scenario, we generate a model absorption profile based on the sum of a minimum number, n_c, of Voigt profiles necessary to explain the observed kinematic signatures. The model depends on a set of free parameters, including for each component the velocity offset with respect to the systemic redshift of the galaxy ($\Delta\, v_c$), the Mg II absorption column density, $\log N_c$(Mg II), and Doppler parameter, b_c, necessary to define the Voigt profile. We then convolve the model profile with a Gaussian function that is appropriate for simulating the instrument resolution offered by MIKE/MagE. We bin the convolved model spectrum to match the size of the spectral pixel in the data. We then compare the binned model spectrum with the observed absorption spectrum and its corresponding error spectrum, and calculate the χ^2. Finally, we constrain the model parameters by minimizing the χ^2.

We note that because the absorption spectra are undersampled and many components are saturated (see Figure 4 for examples), N_c(Mg II) and b_c are not well constrained and serve only as a guide. On the other hand, the velocity centroid of each identified component is well determined to be better than a small fraction of the resolution element (~ 2 km s^{-1}), which is the key measurement necessary for constructing an accurate 3D velocity map.

Next, we characterize the observed absorption as due to density fluctuations in the Mg^+ ions and measure the effective optical depth $\tau_{\rm eff}$ as a function of line-of-sight velocity offset $\Delta\, v$. The effective optical depth is defined as

$$\tau_{\rm eff} = -\ln \langle\, F \,\rangle \equiv -\ln \langle\, e^{-\tau} \,\rangle, \quad (1)$$

where τ is the underlying Mg II optical depth and $\langle\, F \,\rangle$ is the mean continuum-normalized flux per pixel. We compute $\tau_{\rm eff}$ using the best-fit model from the Voigt profile analysis described above to avoid saturated pixels or pixels with negative fluxes. The observed $\tau_{\rm eff}$ provides a simple and non-parametric characterization of how the mean Mg II absorption varies with $\Delta\, v$ along individual sightlines. It does not depend on detailed assumptions of the number of absorption clumps that may be blended in each observed absorption component. We also compute the optical depth-weighted mean velocity offset, $\Delta\, v_\tau$, and the velocity width that encloses 90% of the total line-of-sight effective optical depth, $\delta\, v_{90}$, for quantifying the line-of-sight gas kinematics. Because $\Delta\, v_\tau$ is calculated based on the effective optical depth per pixel, the uncertainties in $\Delta\, v_\tau$ is approximately the pixel resolution of the data, which is 10 km s^{-1} for MIKE and 40 km s^{-1} for MagE spectra.

4.2 Spatially Resolved Halo Gas Kinematics around the Blue Star-forming Galaxy $G1$ at $z = 0.4188$

Absorption kinematics of halo gas around the L_* galaxy $G1$ is displayed in Figure 4, which shows the Mg II $\lambda\lambda$ 2796,2803 absorption profiles observed along the four lensed QSO sightlines. The zero relative velocity in each panel corresponds to the systemic redshift of the galaxy at $z = 0.4188$. The best-fit model spectrum of each sightline (obtained following the procedures described in § 4.1) is also presented in red for comparison. The observations have uncovered a relatively uniform coverage of Mg II absorbing gas at ~ 50 projected kpc from the star-forming disk, with all four sightlines displaying a strong Mg II absorber of $W_r(2796) \gtrsim 1$ Å. In addition, while individual components along individual sightlines are observed to spread over a large velocity range, ~ 160 km s^{-1} along the sightline toward the B image and ~ 140 km s^{-1} toward C, the absorption morphology appears to be remarkably similar across these sightlines with a dominant absorption pair occuring near the systemic redshift of $G1$ and trailed by a second pair of absorption features at $\approx +110$ km s^{-1}. Only a relatively small velocity shear ($\Delta\, v \approx 20$ km s^{-1}) is seen between different sightlines that are separated by $8 - 10$ kpc in projected distances.

As described in § 3.1, $G1$ is a typical blue star-forming galaxy at $z = 0.4188$ and ~ 50 kpc in projected distance from the quad-lens system. The galaxy has a fainter companion at ≈ 120 kpc in projected distance *farther* away from the QSO sightlines. The star-forming disk of $G1$ is characterized by an inclination angle of $i_0 = 40^\circ$ and position angle of P.A. $= 173^\circ$ measured north through east. In Table 2, we list for each sightline the angular separation between $G1$ and each QSO image $\theta_{\rm qim}$, the corresponding projected distance ρ, the azimuthal angle α of the QSO sightline with respect to the major axis of the star-forming disk, the rest-frame absorption equivalent width intergrated over all components $W_r(2796)$, the optical depth-weighted mean velocity offset $\Delta\, v_\tau$, the velocity width that encloses 90% of the total line-of-sight effective optical depth, $\delta\, v_{90}$, the number of components n_c necessary to reproduce the observed absorption profile along each sightline, and the respective best-fit Voigt profile parameters of each Mg II absorbing component [$\Delta\, v_c$, $\log N$(Mg II), b_c]. Given the observed $W_r(2796)$, we further estimate a chemical enrichment level of $f_Z = 0.1 - 0.4$ solar metallicity for the Mg II absorbers around $G1$ based on the redshift-corrected metallicity–$W_r(2796)$ relation of Murphy et al. (2007). Including the scatter observed by Murphy et al. (2007), the gas metallicity can be as high as 0.9 solar and as low as 0.05 solar.

Combining known orientation of the quadruply-lensed QSOs to $G1$ from available HST images with the observed Mg II $\lambda\lambda$ 2796,2803 absorption profiles along individual QSO sightlines leads a 3D velocity map of halo gas around the galaxy. The top panel of Figure 5 shows the relative orientation of the quadruply-lensed QSO to $G1$ at $\rho \sim 50$ kpc. The spectral images in the bottom of Figure 5 display the effective optical depth $\tau_{\rm eff}$ of Mg II versus line-of-sight velocity offset from $z = 0.4188$ (the systemic redshift of $G1$). The values of $\tau_{\rm eff}$ are indicated by the color bar in the

Table 2. Spatial Variation of Mg II Absorption Properties[a] around $G1$ at $z = 0.4188$

Sightline[b]	$\theta_{\rm qim}$ ($''$)	ρ (kpc)	α^c (°)	$W_r(2796)$ (Å)	$\Delta\, v_\tau$ (km s^{-1})	$\delta\, v_{90}$ (km s^{-1})	n_c	component	$\Delta\, v_c$ (km s^{-1})	log N_c(Mg II)	b_c (km s^{-1})
A	9.7	53.6	119	1.1 ± 0.1	+76	169	3	1	+26	13.1	19
								2	+64	13.4	19
								3	+153	13.1	13
B	8.1	44.7	120	1.9 ± 0.1	+32	185	4	1	−23	13.7	27
								2	+19	14.0	27
								3	+96	13.2	27
								4	+135	13.5	27
C	7.8	43.1	130	1.5 ± 0.1	+18	163	4	1	−11	14.2	15
								2	+41	13.4	15
								3	+95	12.8	20
								4	+125	12.5	20
D	9.6	53.0	130	1.0 ± 0.1	+54	161	2	1	+22	13.6	22
								2	+112	13.1	22

[a]Due to a heavy binning in the data, N_c(Mg II) and b_c are not well constrained in the Voigt profile analysis and serve only as a guide.
[b]The projected distances between different sightlines are $(\overline{\rm AB}, \overline{\rm AC}, \overline{\rm AD}, \overline{\rm BC}, \overline{\rm BD}, \overline{\rm CD}) = (8.8, 13.8, 10.3, 8.2, 12.2, 10.0)$ kpc.
[c]Azimuthal angle of the QSO sightline from the major axis of the star-forming disk (measured counterclockwise).

lower-left corner. We note that the projected distances between different sightlines are $(\overline{\rm AB}, \overline{\rm AC}, \overline{\rm AD}, \overline{\rm BC}, \overline{\rm BD}, \overline{\rm CD}) = (8.8, 13.8, 10.3, 8.2, 12.2, 10.0)$ kpc. From the inner sightlines B and C at $\rho \approx 45$ kpc (bottom two spectral images) to the outer ones A and D at $\rho \approx 55$ kpc (top two spectral images), we observe a consistent increase in the relative velocity offsets of regions where dominant absorption occurs. The spatial coherence between four different sightlines, as evident from both the absorption signatures presented in Figure 4 and the velocity shears displayed in Figure 5, strongly suggests that the absorbing gas follows an organized motion.

4.3 Spatially Resolved Halo Gas Kinematics around the Quiescent Star-forming Galaxy $G2$ at $z = 0.7818$

Absorption kinematics of halo gas around the super-L_* galaxy $G2$ is displayed in Figure 6, which shows the Mg II $\lambda\lambda$ 2796,2803 absorption profiles observed along three of the four QSO sightlines. The zero relative velocity in each panel corresponds to the systemic redshift of the galaxy. Recall that the Mg II absorption doublet associated with $G2$ occur near the cross-over wavelength of the dichroic in MIKE where the S/N of the spectra is particularly poor. Only moderate-resolution MagE spectra are available for detecting the Mg II absorption feature at this redshift. In every panel, the continuum normalized absorption spectrum is shown in black solid histograms with contaminating features dotted out and the corresponding 1-σ error spectrum shown in thin cyan. The best-fit model spectrum of each sightline that takes into account the spectral resolution of the instrument as described in § 4.1 is also presented in red for comparison.

Similar to $G1$, the observations have uncovered a relatively uniform coverage of Mg II absorbing gas at ~ 30 projected kpc from the barred spiral, with all three sightlines showing the presence of Mg II absorption. In contrast to $G1$, however, the gaseous halo around $G2$ displays only a moderately strong Mg II absorber of $W_r(2796) = 0.5 - 0.7$ Å along these sightlines at smaller projected distances from the galaxy. The observed $W_r(2796)$ implies a low chemical enrichment level of $f_Z = 0.06$ solar metallicity for the Mg II absorbers around $G2$ based on the redshift-corrected metallicity–$W_r(2796)$ relation of Murphy et al. (2007). Including the scatter observed by Murphy et al. (2007), the gas metallicity can be as high as 0.15 solar and as low as 0.01 solar. In addition, despite a lower spectral resolution, the MagE data show remarkably distinct absorption morphology across different sightlines. In particular for C' and D' (after lensing correction at $z = 0.7818$; see the image in Figure 7) at a similar projected distance from $G2$ and roughly 6 kpc apart, the observed Mg II absorption is spread over 130 km s^{-1} along the sightline toward C', whereas more concentrated absorption is found within a narrow FWHM ≈ 42 km s^{-1} along the sightline toward D'.

As described in § 3.2, $G2$ is a massive, quiescent star-forming galaxy at $z = 0.7818$ and ~ 30 kpc in projected distance from the quad-lens system. No companion is known for this galaxy. The star-forming disk of $G2$ is nearly face-on with an inclination angle of $i_0 = 25°$ and position angle of P.A. $= 13°$ measured north through east. In addition, $G2$ occurs behind the lensing galaxy at $z_{\rm lens} = 0.4546$ and the angular separations observed between lensed QSO images only apply to objects at $z \lesssim z_{\rm lens}$. Assuming that the QSO is located directly behind the lens[1], we compute the lensed image positions at the $z = 0.7818$ plane through ray tracing.

[1] We note that Morgan et al. (2005) find that a lens model should include shear from neighboring galaxies in order to simultaneously reproduce the observed locations *and* flux ratios of the lensed quasar. With shear included, the unknown source position is found by the best-fit model to be $0.14''$W and $0.13''$S from the center of the lens (The best-fit parameters were generously provided to us by C. Kochanek, private communication). Assuming this source position, the impact parameters we report in Table

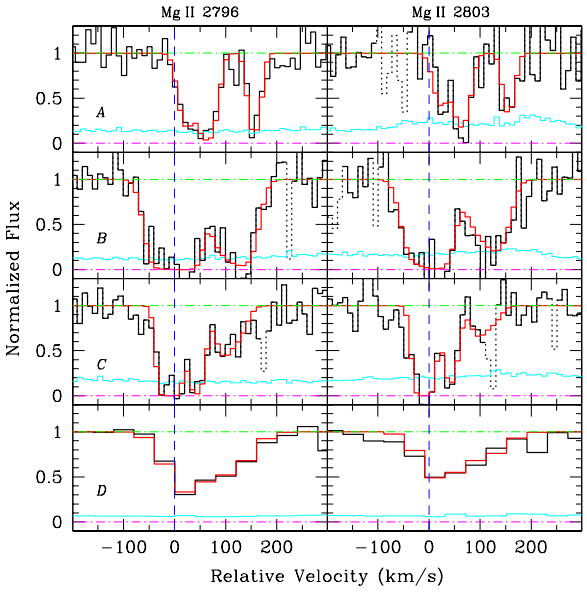

Figure 4. Mg II $\lambda\lambda$ 2796,2803 absorption profiles along four different sightlines through the halo around the L_* galaxy $G1$ at $z = 0.4188$. Zero relative velocity corresponds to the systemic redshift of the galaxy. In every panel, the continuum normalized absorption spectrum is shown in black solid histograms with contaminating features dotted out for clarification, and the corresponding 1-σ error spectrum is shown in thin cyan. The absorption spectra of A, B, and C are from the high-resolution MIKE observations, while the spectrum of D is from MagE (§ 2.3). The red spectrum shows the best-fit model (with a reduced $\chi^2 \approx 2$), which takes into account the instrument resolution and pixel binning during readout (§ 4.1). The Mg II absorption doublet is generally characterized by a dominant component near the systemic velocity, which is followed by secondary absorbing components at ~ 100 km s^{-1} in the red. Such kinematic signatures apply to all four sightlines separated by $8-10$ kpc in projected distances, and only a relatively small velocity shear (between $\Delta v \approx 20$ km s^{-1}) is seen across these different sightlines.

The results are shown as green stars in the top panel of Figure 7.

The top panel of Figure 7 displays the relative orientation of the quadruply-lensed QSO to $G2$. We have combined a high-contrast image of the lensed QSOs with an image of $G2$ which is adjusted to emphasize the spiral structures. The relative spatial scale remains the same as what is shown in Figure 1. The green star symbols indicate where the light from the QSO crosses the plane of $G2$. We designate the lensing corrected image positions as A', B', C', and D'. In Table 3, we list for each sightline the lensing-modified angular distance of $G2$ to the QSO image $\theta_{\rm qim}$ at the $z = 0.7818$, the corresponding projected distance ρ, the azimuthal angle α of the QSO sightline with respect to the major axis of the star-forming disk, the rest-frame absorption equivalent width intergrated over all components $W_r(2796)$, the optical depth-weighted mean velocity offset Δv_τ, the velocity width

3 and § 4.3 change by less than 1 kpc, which does not affect the results reported in this paper.

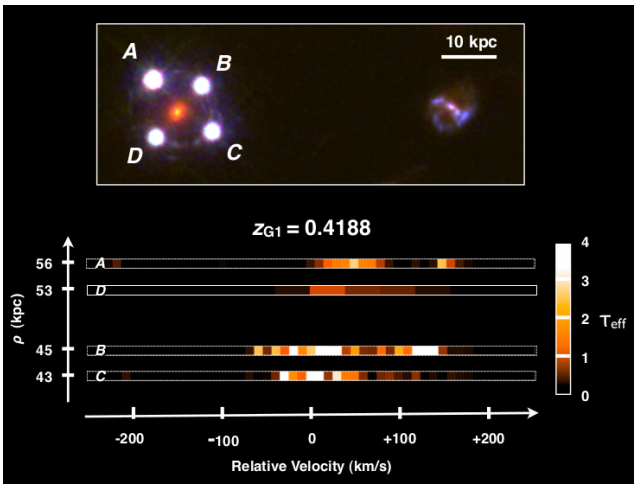

Figure 5. Spatially resolved halo gas kinematics around the L_* galaxy $G1$ at $z = 0.4188$. The top panel shows the relative orientation of the quadruply-lensed QSO to $G1$ at $\rho \sim 50$ kpc. The spectral images at the bottom display the effective optical depth $\tau_{\rm eff}$ of Mg II versus line-of-sight velocity offset from $z = 0.4188$ (the systemic redshift of $G1$) for individual sightlines with increasing projected distance ρ from bottom to top. The values of $\tau_{\rm eff}$ are indicated by the color bar in the lower-left corner. Note that the projected distances between any two sightlines are very similar, ~ 10 kpc. The apparent velocity shear is found to be ~ 40 km s^{-1} between A and B or between C and D with increasing ρ, while a velocity difference of $\lesssim 20$ km s^{-1} is seen between A and D or between B and C that are at similar projected distances.

that encloses 90% of the total line-of-sight effective optical depth, δv_{90}, the number of components n_c necessary to reproduce the observed absorption profile along each sightline, and the respective best-fit Voigt profile parameters of each component [Δv_c, log N(Mg II), b_c].

Combining known orientation of the QSO images to $G2$ with the observed Mg II $\lambda\lambda$ 2796,2803 absorption profiles along individual QSO sightlines leads a 3D velocity map of halo gas around the galaxy. The spectral images in the bottom of Figure 7 display the effective optical depth $\tau_{\rm eff}$ of Mg II versus line-of-sight velocity offset from $z = 0.7818$ (the systemic redshift of $G2$). The values of $\tau_{\rm eff}$ are indicated by the color bar in the lower-left corner. We note that the projected distances between different lensed sightlines at $z = 0.7818$ are $(\overline{A'C'}, \overline{A'D'}, \overline{C'D'}) = (7.8, 5.7, 5.7)$ kpc. In constrast to the halo around $G1$, the absorbers uncovered along sightlines at smaller projected separations from $G2$ show distinct velocity structures with a difference in the mean velocity of ≈ 90 km s^{-1}. Such distinct line-of-sight velocity distributions suggests a turbulent halo gas near the star-forming disk of $G2$.

5 DISCUSSION

Combining known orientations of the quadruply-lensed QSOs to two foreground galaxies with the observed Mg II $\lambda\lambda$ 2796,2803 absorption profiles along individual QSO sightlines has allowed us for the first time to resolve the kinematics of tenuous halo gas on scales of $5-10$ kpc at $z > 0.2$ (cf. Verheijen et al. 2007). We detect a Mg II absorber in

Table 3. Spatial Variation of Mg II Absorption Properties[a] around $G2$ at $z = 0.7818$

Sightline[b]	$\theta_{\rm qim}$ ($''$)	ρ (kpc)	α^c (°)	$W_r(2796)$ (Å)	$\Delta\, v_\tau$ (km s^{-1})	$\delta\, v_{90}$ (km s^{-1})	n_c	component	$\Delta\, v_c$ (km s^{-1})	log N_c(Mg II)	b_c (km s^{-1})
A'	4.9	36.8	26	0.51 ± 0.03	+187	280	2	1	+123	12.8	91
								2	+258	12.8	23
C'	4.1	31.0	16	0.72 ± 0.03	+97	280	2	1	+57	13.2	61
								2	+185	12.9	20
D'	4.2	31.1	27	0.56 ± 0.04	+36	102	1	1	+35	13.3	25

[a]With a moderate spectral resolution, N_c(Mg II) and b_c are not well constrained in the Voigt profile analysis and serve only as a guide.
[a]The projected distances between different lensed sightlines at $z = 0.7818$ are $(\overline{A'C'}, \overline{A'D'}, \overline{C'D'}) = (7.8, 5.7, 5.7)$ kpc.
[b]Azimuthal angle of the QSO sightline from the major axis of the star-forming disk (measured counterclockwise).

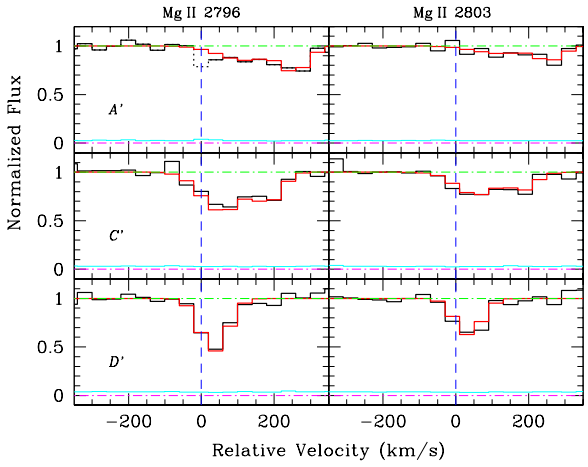

Figure 6. Mg II $\lambda\lambda$ 2796,2803 absorption profiles of halo gas around the super-L_* barred spiral galaxy $G2$ at $z = 0.7818$. Absorption spectra of QSO sightlines A', C', and D' (corrected lensed image positions at the redshift plane of $G2$; see the image in Figure 7) obtained with MagE are available. Zero relative velocity corresponds to the systemic redshift of the galaxy at $z = 0.7818$. Despite a lower spectral resolution, the MagE spectra show remarkably distinct absorption morphology across different sightlines. In particular, sightlines C' and D' occur at a similar projected distance from $G2$ and are roughly 6 kpc in projected separation. The observed Mg II absorption is spread over 130 km s^{-1} along the sightline toward C', whereas more concentrated absorption is found within a narrow FWHM $\approx$ 42 km s^{-1} along the sightline toward D'.

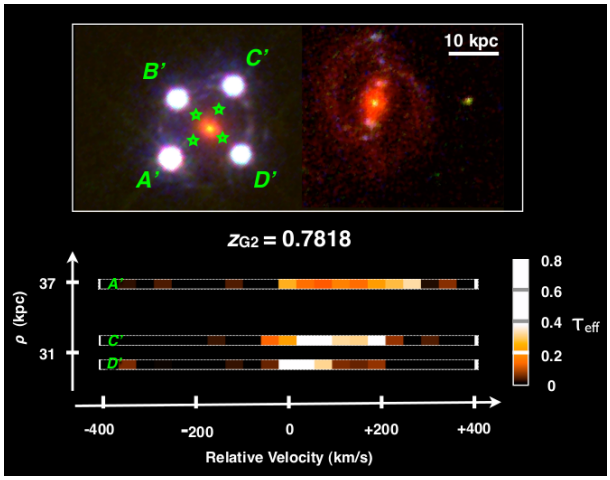

Figure 7. Spatially resolved halo gas kinematics around the super-L_*, barred spiral galaxy $G2$ at $z = 0.7818$. The top panel shows the relative orientation of the quadruply-lensed QSO to $G2$ at $\rho \sim 30$ kpc. We have combined a high-contrast image of the lensed QSOs with an image of $G2$, adjusted to emphasize the spiral structures. The relative spatial scale remains the same as what is shown in Figure 1. In addition, because $G2$ is located behind the lens, the actual angular separations between the lensed QSO sightlines are smaller than what are marked by the lensed QSO images. The green star symbols indicate where the light from the QSOs crosses the $z = 0.7818$ plane. Similar to Figure 5, the spectral images at the bottom display the effective optical depth $\tau_{\rm eff}$ of Mg II versus line-of-sight velocity offset from $z = 0.7818$ (the systemic redshift of $G2$) for individual QSO sightlines (with increasing projected distances ρ from bottom to top). The values of $\tau_{\rm eff}$ are indicated by the color bar in the lower-left corner. The projected distances between $\overline{A'D'}$ and $\overline{C'D'}$ are comparable, which are $\sim$ 6 kpc. But similar to what is found for the halo of $G1$, a larger velocity shear is seen with increasing ρ than at comparable ρ.

every sightline through the halo of each of the two galaxies in our study. The absorber strength observed in these galaxies is typical of what is seen in previous close QSO–galaxy pair studies (e.g. Chen et al. 2010a,b). While both galaxies confirm previously reported high covering fraction of Mg II absorbing gas at $\rho < 50$ kpc from star-forming disks, they also present two contrasting examples of the complex halo gas dynamics.

For $G1$, a likely member of a loose group as suggested by a neighboring galaxy at a projected distance of 120 kpc away, a strong Mg II absorber of $W_r(2796) > 1$ Å is present in all four sightlines at $\approx$ 50 kpc from the star-forming disk. The absorbers from different sightlines that are $\sim$ 10 kpc apart in projected separations share a similar asymmetry in their absorption profiles. We show a stacked halo velocity profile in the top panel of Figure 8, which is established by coadding the observed effective optical depth of Mg II along four different sightlines through the halo of $G1$. The coadded velocity profile is clearly inconsistent with a Gaussian distribution, likely indicating that the absorbing gas is not distributed randomly in the halo. In addition, the velocity width that encloses 90% of the total line-of-sight effective optical depth is $d\, v_{90} \approx 170$ km s^{-1} across all four sightlines with a steady increase of $\Delta\, v_\tau$ from small (B and C) to large

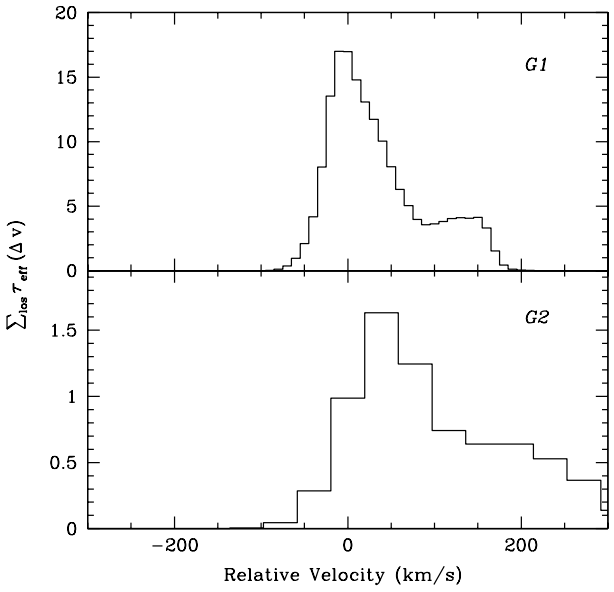

Figure 8. Collective velocity profiles of the gaseous halos around $G1$ (top) and $G2$ (bottom) from coadding the observed effective optical depth of Mg II versus velocity offset along different sightlines through each halo. Same as Figures 4 and 6, the zero velocity in each panel corresponds to the systemic redshift of the associated galaxy. The coadded velocity profiles from multiple sightlines are not a Gaussian function, indicating that the absorbing gas is not distributed randomly in each halo.

(A and D) projected distances ρ. Therefore, not only does the absorbing gas appear to be deviating from a uniformly distributed halo, but there also exists a strong spatial coherence between these four sightlines.

In contrast, a moderately strong Mg II absorber of $W_r(2796) \approx 0.6$ Å is detected in all three observed sightlines at ≈ 30 kpc from $G2$, a barred spiral galaxy. The Mg II absorbers uncovered along individual sightlines that are ~ 6 kpc apart in projected separations exhibit distinct absorption signatures, from a relatively more concentrated single component found along the sightline toward the D' image with $\Delta\, v_\tau = +36$ km s^{-1} and $\delta\, v_{90} = 102$ km s^{-1}, to widely separated multiple components with $\Delta\, v_\tau \gtrsim 100$ km s^{-1} and $\delta\, v_{90} = 280$ km s^{-1}. While MagE delivers a spectral resolution of ≈ 70 km s^{-1} and therefore the intrinsic width of the single-component absorber uncovered along the D' sightline is likely to be < 102 km s^{-1}, the larger $\delta\, v_{90}$ seen along the sightlines toward A' and C' (which is four times the resolution element) can only be driven by the underlying gas kinematics along these sightlines. The vastly different $\Delta\, v_\tau$ and $\delta\, v_{90}$ along these three sightlines separated by < 10 kpc indicate a turbulent velocity field near $G2$.

The rich data set allows us to begin to constrain theoretical models for inflows and galactic-scale outflows. Here we examine different models by comparing the observed 3D map of gaseous halos with model expectations. We also discuss the implications of our finding in the general understanding of halo gas dynamics from absorption-line observations.

5.1 Gas Flow Models

We examine different gas flow models by comparing the observed 3D map of gaseous halos with model expectations. Three models are considered here: (1) a rotating gaseous disk; (2) collimated outflows; and (3) infalling streams or tidally stripped gas.

5.1.1 A rotating gaseous disk

We first consider the possibility that the gas probed by the Mg II absorption follows the rotational motion of the star-forming disk (e.g. Steidel et al. 2002; Chen et al. 2005). Under this scenario, the observed line-of-sight velocity offsets between different QSO sightlines are interpreted as a result of velocity gradient along the rotating disk. Given the well-resolved optical morphologies of galaxies $G1$ and $G2$, we are able to determine the disk inclination (i_0) and orientation (α) relative to each QSO sightline and deproject the observed line-of-sight velocity to the plane along the stellar disk. Following Chen et al. (2005), the projected distance ρ is related to galactocentric radius R according to

$$\frac{R}{\rho} = \sqrt{1 + \sin^2\alpha\, \tan^2 i_0}, \tag{2}$$

and the line-of-sight velocity $v_{\rm los}$ is related to the rotation speed $v_{\rm rot}$ along the disk according to (see Steidel et al. 2002 for an alternative expression)

$$v_{\rm rot} = \frac{v_{\rm los}}{\cos\alpha\, \sin i_0} \sqrt{1 + \sin^2\alpha\, \tan^2 i_0}. \tag{3}$$

Equations (2) and (3) reduce to $R = \rho$ and $v_{\rm rot} = v_{\rm los}/\sin i_0$, when the sightline intercepts the major axis ($\alpha = 0$).

For $G1$, sightlines A and B share a similar α and therefore offer a direct measure of velocity gradient along the disk. The observed projected distance between A and B of $\overline{\rm AB} = 8.8$ kpc leads to a deprojected distance of $R_{AB} = 10.9$ kpc along the stellar disk. The observed line-of-sight velocity difference, $\Delta\, v_\tau(A) - \Delta\, v_\tau(B) = 44 \pm 14$ km s^{-1}, leads to an increase in the rotation speeds of $dv_{\rm rot}^{AB} = 169 \pm 46$ km s^{-1} from B to A. Together, we derive a steep velocity gradient of $\partial\, v/\partial\, R = 16 \pm 4$ km s^{-1} per kpc at $R > 55$ kpc. Similarly, sightlines C and D have the same α. With $R_{CD} = 11.8$ kpc and $dv_{\rm rot}^{CD} \approx 104$ km s^{-1}, we derive $\partial\, v/\partial\, R \approx 9$ km s^{-1} per kpc at $R > 50$ kpc. The velocity gradient would be even steeper, when considering the velocity shear seen between B and C or between A and D that occur at comparable galactocentric radii. While large gaseous disks of radius > 50 kpc are known to exist, these galaxies also show a flat rotation curve beyond the optical disks (e.g. Sofue & Rubin 2001; Lelli et al. 2010).

A simple rotating disk cannot explain the velocity map around $G2$, either. It is immediately clear that C' and D' occur at the same projected distance to the star-forming disk and yet the absorbers display a line-of-sight velocity difference of 60 km s^{-1}. Considering only component 1 along sightline C' at $\Delta\, v_c = +57$ km s^{-1} would still lead to a line-of-sight velocity difference of 22 km s^{-1} between C' and D' at the same $\rho = 31$ kpc. The inferred velocity gradient along the stellar disk between D' and A' would also be enormous $\partial\, v/\partial\, R > 60$ km s^{-1} per kpc at $R > 30$ kpc. Therefore, we conclude that the gas kinematics revealed by the Mg II

absorption around either $G1$ or $G2$ is inconsistent with expectations of a rotating disk.

5.1.2 Bi-conical outflows

Next, we consider the popular scenario that Mg II absorbers detected in random QSO sightlines originate in supergalactic winds (e.g. Bouché et al. 2006; Chelouche & Bowen 2010; Ménard et al. 2011; Nestor et al. 2011). In the local universe, large-scale galactic outflows are commonly seen to follow a bi-conical pattern along the rotation axis of the star-forming disk (e.g. Heckman et al. 2000) with a varying degree of collimation, typically $2\,\theta_0 = 45^\circ - 100^\circ$ above the disk (Bland-Hawthorn, Veilleux & Cecil 2007). This is understood as the outflowing gas moves along the path of least resistance. In addition, observations of local starburst galaxies have shown that galactic-scale superwinds exist in galaxies with a global star formation rate per unit area exceeding $\sum_{\rm SFR} = 0.1$ M$_\odot$ yr^{-1} kpc^{-2} (Heckman 2002). Of the two galaxies identified in the foreground of HE 0435−1223, $G1$ has an unobscured star formation rate per unit area of $\sum_{\rm SFR}(G1) \approx 0.06$ M$_\odot$ yr^{-1} kpc^{-2} after correcting for the disk inclination, and $G2$ has $\sum_{\rm SFR}(G2) \approx 0.002$ M$_\odot$ yr^{-1} kpc^{-2}. It is therefore possible that supergalatic winds are present in at least $G1$, if dust extinction is significant.

Gauthier & Chen (2012) developed an analytic formalism to fully characterize the velocity gradient along biconical outflows based on observed absorption profiles. By attributing the observed line-of-sight velocity spread to the intrinsic velocity gradient along collimated outflows, these authors demonstrated that the outflow velocity field can be uniquely established from absorption-line data, when the outflow opening angle θ_0, and the inclination (i_0) and orientation (α) angles of the star-forming disk are known. They applied this analytic model to three edge-on disk galaxies that have a background QSO probe the halo gas near the minor axis. The combination of highly inclined disks and a QSO ocurring near the minor axis together helped tighten the constraints on the outflow velocity field even with a single QSO sightline. Gauthier & Chen (2010) showed that it is difficult for accelerated outflows (e.g. Martin & Bouché 2009; Steidel et al. 2010; Murray et al. 2011) to provide a general explanation for the strong Mg II absorbers observed near the minor axis around the galaxies in their study.

Following Gauthier & Chen (2012), we assume that the observed Mg II absorbers in the quad-lens sightlines originated in collimated outflows from the foreground galaxies $G1$ and $G2$, and derive the velocity gradient necessary to explain the observed velocity shear between different sightlines. An important gain in our study here is the available absorption profiles from multiple sightlines for each galaxy. An alternative model to collimated outflows is expanding shells (e.g. Rauch et al. 2002) that resembles wind-blown bubbles (e.g. Heiles 1979). This alternative model is disfavored here due to a lack of symmetry in the absorption profiles (cf. Bond et al. 2001) between different sightlines about the systemic redshift of the galaxies.

We first constrain θ_0 (defined as half of the angular span of the collimated outflows, see Figure 9) based on known inclination and orientation angles of the disk and the observed relative velocity offsets of different Mg II absorption components along different lensed QSO sightlines. We have shown that the star-forming disk of $G1$ has $i_0 = 40^\circ$, $\alpha = 120^\circ$ for sightlines A and B, and $\alpha = 130^\circ$ for sightlines C and D. A strong Mg II absorber is found in every one of the four sightlines. With the modest inclination of the disk and the sightlines intercepting the halo at $\rho \approx 50$ kpc and $30^\circ - 40^\circ$ from the minor axis, we derive a minimum θ_0 of $\theta_0^{\rm min}(G1) \approx 30^\circ$ in order for the collimated outflows to intercept all four sightlines. The maximum opening angle of the outflows for $G1$, $\theta_0^{\rm max}(G1)$, is more uncertain, because of the complex velocity distribution of individual components along different sightlines. Recall that no blueshifted components are detected along the sightlines toward A and D and the dominant absorption along sightlines B and C occurs near the systemic redshift of the star-forming disk at $\rho \approx 45$ kpc (Figure 4 and Table 2). Under a simple assumption that the outflowing gas is uniformly distributed in the cone, the lack of blueshifted components toward A and D would lead to $\theta_0^{\rm max}(G1) \lesssim 55^\circ$, while the presence of blueshifted components toward B and C would lead to $\theta_0^{\rm max}(G1) \gtrsim 55^\circ$ (Figure 9). In particular, because A and B occur at the same α, it is expected that a continuous stream moving outward and intercepting sightline B to produce the blueshifted component at $\Delta\,v_c = -23$ km s^{-1} would continue to move on to intercept sightline A at a similar $\Delta\,v_c$ but the first absorbing component seen in sightline A is nearly +50 km s^{-1} away. The same caveat is seen C and D which share a similar $\alpha = 130^\circ$. *If the blueshifted components seen in B and C arise in outflows that are moving toward the observer, then the outer layers of the collimated outflows are expected to be disrupted at $\rho \lesssim 50$ kpc* before reach out to distances probed by A and D. However, some outflowing gas would still have to move beyond 50 kpc in order to produce the redshifted components see in A and D. *This would imply an increasing degree of collimation in the outflows with increasing distance.* Alternatively, the blueshifted components observed in sightlines B and C may not be associated with galactic winds. If attributing only redshifted components in all four sightlines as due to outflows, then we can constrain the opening angle with $\theta_0^{\rm max}(G1) \lesssim 55^\circ$.

For $G2$, we found that $i_0 = 25^\circ$ for the disk, and $\alpha = 26^\circ$ for sightlines A' and D', and $\alpha = 16^\circ$ for sightline C'. With a nearly face-on disk and the sightlines intercepting the halo at $\rho \approx 30$ kpc and $\alpha \lesssim 26^\circ$ from the major axis, we derive a minimum θ_0 of $\theta_0^{\rm min}(G2) \approx 56^\circ$ in order for the collimated outflows to intercept all three sightlines. A large θ_0 with $\theta_0 > 65^\circ$ would lead to blueshifted components along sightlines A' and D' at $\rho \gtrsim 30$ kpc, which are not seen. Therefore, the maximum opening angle is constrained based on the absence of blueshifted components at $\theta_0^{\rm max}(G2) \approx 65^\circ$.

Next, we calculate the velocity gradient in the collimated outflows that is necessary to produce the observed velocity shear between different sightlines. Because the relative locations of individual components between different sightlines in the collimated outflows are not known, we compute the velocity gradient based on $\Delta\,v_\tau$, the effective optical depth weighted line center, average over the entire absorber in each sightline. As mentioned earlier, sightlines A and B intercept the halo of $G1$ at a nearly identical azimuthal angle $\alpha = 120^\circ$ from the disk and are roughly 9 kpc apart. It is therefore conceivable that A and B trace the same streams of gas outflowing from the disk at some mean angle θ' from

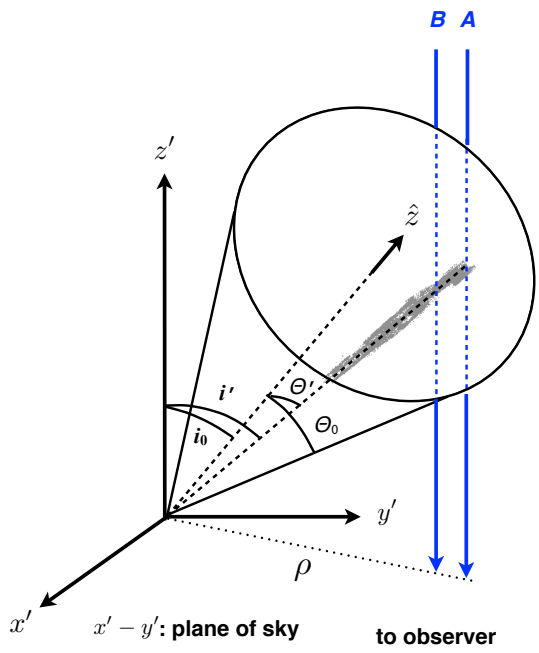

Figure 9. Cartoon illustrating the impact geometry of multiple sightlines intercepting conical outflows. The plane of sky is marked by the $x'-y'$ axes and the z' axis points to distant objects. The outflow is reprepresentd by the cone oriented along the rotation axis $\hat{z}$ with inclination angle i_0 and opening angle $2\times\theta_0$. It is expected from this orientation that when θ_0 is sufficiently large to cross the plane of the sky, the outflows would imprint blueshifted absorption features in the spectra of background sources. A lack of blueshifted components would therefore constrain the maximum θ_0. Within the cone, gas streams move outward at different angle $\theta' \lesssim \theta_0$ from $\hat{z}$ with corresponding inclination angle i' (the thick paint brush line is marked as an example of such outward moving stream). In principle, the velocity gradient along the streams can be directly constrained by the average velocity shears observed between different sightlines (marked A and B) that occur at the same azimuthal angle on the sky (Equation 4).

the disk rotation axis (see Figure 9 for illustrations). But recall the caveat that the blueshifted components uncovered toward B and C may not be associated with outflows, in which case the velocity gradient inferred below would represent an upper limit.

Adopting the analytic conical outflow model of Gauthier & Chen (2012), we convert the line-of-sight velocity gradient to outflow velocity along the rotation axis following

$$\frac{\delta\, v}{\delta\, z} = \frac{\cos i'\, \sin i'}{\cos\theta'}\, \frac{\delta\, v_{\rm los}}{\delta\, \rho}, \tag{4}$$

where $\delta\, v_{\rm los} = \Delta\, v_\tau(A) - \Delta\, v_\tau(B)$, $\delta\, \rho = \rho(A) - \rho(B)$, θ' is the angle of the outflowing stream away from the rotation axis and is related to ρ and α according to

$$\tan\theta' = \frac{\sin i_0 \cos\alpha}{\sin\alpha}, \tag{5}$$

and i' is the corresponding inclination angle of the stream at θ' and is related to ρ and θ' according to

$$\sin i' = \frac{\rho}{z}\cos\theta' = \frac{\sin i_0 \cos\theta'}{\sin\alpha}. \tag{6}$$

Note that $\theta' = 0$ and $i' = i_0$, if $\alpha = 90^\circ$ (namely when the sightlines occur near the minor axis of the disk).

Comparing $\Delta\, v_\tau$ along A and B sightlines leads to a velocity difference of $\delta\, v = +26$ km s^{-1} from 60 kpc to 70 kpc in z-height for an outflowing stream at $\theta' \approx 20^\circ$ from the rotation axis. Likewise, sightlines C and D intercept the halo of $G1$ at $\alpha = 130^\circ$ and are 10 kpc apart. Equation (4) leads to to a velocity difference of $\delta\, v = +20$ km s^{-1} from 50 kpc to 60 kpc in z-height for an outflowing stream at $\theta' \approx 28^\circ$ from the rotation axis. The relatively shallow velocity gradient is comparable to the expected acceleration in radiation pressure driven winds at large distances (e.g. Murray et al. 2011). At the same time, the deprojected outflow speed (~ 100 km s^{-1}) at > 50 kpc above the disk is significantly smaller than expectations from accelerated outflows (e.g. Steidel et al. 2010; Murray et al. 2011), but comparable to expectations for galactic winds driven by cosmic rays (e.g. Booth et al. 2013).

For $G2$, sightlines A' and D' intercept the halo at a nearly identical azimuthal angle $\alpha = 26^\circ$ from the disk and are roughly 6 kpc apart. Considering the Mg II absorbers uncovered in these two sightlines, we calculate the velocity gradient in the collimated outflows based on the observed $\Delta\, v_\tau$ and obtain a steep velocity gradient $\delta\, v/\delta\, z = 18\,{\rm km\ s^{-1}\,/\,kpc}$ at $30 - 40$ kpc above the disk. The inferred velocity gradient exceeds expectations for accelerated outflows at these distances (e.g. Steidel et al. 2010; Murray et al. 2011).

In summary, our analysis shows that a simple outflow scenario alone cannot provide a consistent explanation for *all* absorbing components found in either $G1$ or $G2$. This is qualitatively consistent with the low metallicity ($0.1 - 0.4$ solar for $G1$ and 0.06 solar for $G2$) inferred for the gas based on the observed $W_r(2796)$. Under the assumption that the Mg II absorbers uncovered in the vicinities of these galaxies originate in collimated outflows, we have demonstrated that multiple probes afforded by the quad-lens allow us to constrain both the outflow opening angle and the velocity gradient. The constraints are based entirely on the relative locations between the lensed QSOs and the line-of-sight absorption profiles, without further assumptions for how individual components along different sightlines are associated with one another.

For $G1$, attributing all the observed Mg II components to collimated outflows would require an increased degree of collimation with increasing distance in the outflows. If only the redshifted components in all four sightlines are attributed to collimated outflows, then the outflow opening angle would be constrained by the data to be within $\theta_0 = [30^\circ, 55^\circ]$. In turn, a shallow velocity gradient of $\delta\, v/\delta\, r \lesssim 2\,{\rm km\ s^{-1}\,/\,kpc}$ at $\gtrsim 50$ kpc above the star-forming disk is derived which is comparable to model expectations for supergalactic winds, while the deprojected velocity falls well below the model expectations. Such discrepancy between outflowing speed and the velocity gradient suggests deceleration rather than acceleration in the outflows.

For $G2$, attributing all the observed Mg II components to collimated outflows constrains the outflow opening angle to within $\theta_0 = [56^\circ, 65^\circ]$. The inferred velocity gradient would substantially exceed model expectations, requiring additional energy input at $\gtrsim 30$ kpc above the disk. Taking into account the observed low $\sum_{\rm SFR}$ in $G2$, we therefore

find it unlikely that the a large fraction of Mg II absorbers observed in all three sightlines at > 30 kpc from $G2$ originate in supergalactic winds.

5.1.3 Infalling streams or stripped gas

We have shown that neither rotating disks, nor collimated outflows can provide a single, consistent model for explaining the observed Mg II absorption kinematics along multiple sightlines around $G1$ and $G2$. At the same time, the absorption profiles exhibit a strong spatial coherence on scales of ~ 10 kpc, suggesting the presence of bulk flows in the halos. The bulk flows are characterized for $G1$ by (1) a similar asymmetric absorption profile of comparable velocity width ($\delta\, v_{90} \approx 170$ km s^{-1}) across four different sightlines (Figure 8), (2) a systematic velocity increment of $\delta\, v \approx +40$ km s^{-1} observed from small (B and C at $\rho = 44$ kpc) to large (A and D at $\rho = 54$ kpc) projected distances, as well as (3) a smaller velocity difference (by a factor of ≈ 2) observed between sightlines of similar projected distances and ≈ 10 kpc apart ($\delta\, v_{\rm los}$(BC) $= 14$ km s^{-1} at $\rho \approx 44$ kpc and $\delta\, v_{\rm los}$(AD) $= 22$ km s^{-1} at $\rho \approx 54$ kpc). Similarly for $G2$, a large velocity increment of $\delta\, v \approx +150$ km s^{-1} is observed from small (D' at $\rho = 31$ kpc) to large (A' at $\rho = 37$ kpc) projected distances, and the velocity difference observed between C' and D' at $\rho = 31$ kpc and ≈ 6 kpc apart is a factor of three smaller, with $\delta\, v_{\rm los}(\rm C'D') = 60$ km s^{-1}.

Here we consider a third scenario in which Mg II absorbing gas originates in gaseous streams driven by gravitational forces in the halo. Gaseous streams can be present either due to accretion from the intergalactic medium (IGM) or tidal/ram-pressure stripping from interacting galaxies. We first consider streams accreted from the IGM.

Galaxies are commonly believed to grow in mass by accretion and mergers (e.g. White & Rees 1978). But while renewed emphases (e.g. Kereš et al. 2005, 2009; Birnboim & Dekel 2003; Dekel & Birnboim 2006; Dekel et al. 2009; Fumagalli et al. 2011) have been made on the importance of feeding galaxy growth by cold streams from the IGM, few direct detections of accretion have been reported in distant galaxies (e.g. Rauch et al. 2011; Rubin et al. 2012). Though indirect evidence suggesting co-rotational motion between gas and stellar disks has been reported by various authors (e.g. Steidel et al. 2002; Chen et al. 2005; Kacprzak et al. 2011; Bouché et al. 2013). Although QSO absorbers uncovered in the vicinities of galaxies in principle offer a promising candidate for infalling gas clouds, ambiguities arise when starburst driven outflows are thought to contribute a dominant fraction of these QSO absorbers.

The lack of direct detections of gas accretion has been attributed to a low covering factor ($\sim 10\%$) of cold streams around galaxies (e.g. Faucher-Giguère & Kereš 2011; Fumagalli et al. 2011). In contrast, we have uncovered a Mg II absorber in every observed sightline through each of the two galaxies studied here. Our multi-sightline observations have revealed not only that extended halo gas is clearly present, but also that the rate of incidence in Mg II absorption is qualitatively consistent with being 100% (e.g. Chen et al. 2010a). While the observed 100% covering fraction appears to be discrepant from model expectations for cold accretion, a direct comparison with simulations is difficult due to unknown neutral hydrogen column densities of the gas revealed through Mg II absorption.

On the other hand, the line-of-sight velocity widths ($\delta\, v_{90}$) of the observed Mg II absorbers are roughly consistent with the circular velocity of the halo, which is related to halo mass according to $v_{\rm circ} \sim 144\, M_{12}^{1/3}\, (1+z)^{1/2}$ km s^{-1} with M_{12} representing halo mass in units of $10^{12}\, \rm M_\odot$. $G1$ is estimated to reside in a halo of $10^{12}\, \rm M_\odot$, which at $z = 0.4188$ has $v_{\rm circ} \approx 170$ km s^{-1}. The Mg II absorption profiles along four sightlines near $G1$ show a velocity width of $\delta\, v_{90} \approx 160 - 180$ km s^{-1}. $G2$ is estimated to reside in a halo of $5 \times 10^{12}\, \rm M_\odot$, which at $z = 0.7818$ has $v_{\rm circ} \approx 330$ km s^{-1}. The Mg II absorption profiles along three sightlines near $G2$ show a velocity width of $\delta\, v_{90} \approx 100 - 280$ km s^{-1}. Therefore, gravitation motion of infalling streams through the halo can explain the observed velocity widths in Mg II absorption.

Alternatively, gaseous streams can be present due to tidal interactions (e.g. Yun et al. 1994; Putman et al. 1998) or ram-pressure stripping (e.g. Lin & Faber 1983). In particular, $G1$ has a known neighboring galaxy at a projected distance of 120 kpc away (§ 3.1), and available HST images show features resembling tidal debris at $\approx 3''$ south and $\approx 2''$ northwest of $G1$ (Figure 1; Morgan et al. 2005). Detailed H I maps of nearby galaxy groups from 21 cm observations (e.g. Yun et al. 1994; Hunter et al. 1998; Chynoweth et al. 2008; Mihos et al. 2012) have revealed extended H I gas covering a large fraction of the area within radius ≈ 50 kpc from the star-forming disk, and the relative velocities of the tidal arms are found to span a range of $\approx \pm 200$ km s^{-1} from the systemic redshift of the galay group. Given the dynamic range of gas motion in stripped gas, we expect to find a mean velocity spread of ~ 230 km s^{-1} projected along a random sightline which is consistent with what is measured for the Mg II absorbers.

In summary, the modest velocity widths $\delta\, v$ of Mg II absorbers observed along multiple sightlines are consistent with the expectations of absorption produced either by infalling streams from the IGM or by stripped gas from tidal interaction or ram pressure. We note that a modest velocity width is also expected for absorption due to recycled winds (e.g. Oppenheimer et al. 2010), but *it is not clear whether recycled winds can explain the asymmetric absorption profiles observed both along individual sightlines and in coadded spectra* (Figure 8). It appears that the gas kinematics revealed along multiple sightlines around $G1$ and $G2$ are best described by gaseous streams of $d_s \gtrsim 10$ kpc in width.

5.2 Implications

We have considered three different scenarios, (1) a rotating gaseous disk, (2) collimated outflows, and (3) infalling streams or stripped gas, as possible explanations for the observed Mg II absorbers along multiple sightlines around $G1$ and $G2$. We find that attributing the observed line-of-sight velocity differences across multiple sightlines to a rotating disk would imply an unreasonably steep velocity gradient at > 50 kpc. A rotating disk model is therefore ruled out. At the same time, collimated outflows cannot fully explain the observed velocity distribution across multiple sightlines. While it is conceivable that some fraction of the observed absorption components originate in collimated outflows with

the rest originating in gas infall, the inferred energetics is significantly lower than expectations for supergalactic winds driven by young stars (but comparable to cosmic-ray driven winds). In contrast, gaseus streams of $d_s \gtrsim 10$ kpc in width due to either accretion from the IGM or tidal/ram-pressure stripping offer the best model to fully explain the gas kinematics revealed by the observed Mg II absorption profiles. We also note that the inferred metal enrichment level (between 0.06 and 0.4 solar) of the Mg II gas from $W_r(2796)$ is also significantly smaller than super-solar metallicity expected for the interstellar medium of massive galaxies with $M_* > 2 \times 10^{10}\,\mathrm{M}_\odot$ (e.g. Savaglio et al. 2005), but consistent with expectations for infalling streams or stripped gas from satellites or the outskirts of a star-forming disk.

Here we discuss the implications of our observations for infall models. Specifically, we focus on the turbulence and mass flow rate in infalling streams.

5.2.1 Turbulence in gaseous halos

While gaseous streams from either accretion or tidal debris provide a promising explanation for the observed velocity widths and relative motion between different sightlines, a clear discrepancy between the observations and model expectations is the gas covering fraction. Specifically, the covering fraction of infalling material is expected to be low, $\sim 10\%$, through out galactic halos (e.g. Faucher-Giguère & Kereš 2011; Fumagalli et al. 2011). This is in contrast to the occurrence of a relatively strong Mg II absorber in every observed sightline through the two galaxies in our study.

A potential explanation for the discrepancy between observations and simulation predictions is turbulence. Whether or not the streams are turbulent is assessed by the Reynolds number (Re) of the flows. For photo-ionized gas at temperature $T \sim 10^4$ K that is expected for infalling streams (e.g. van de Voort & Schaye 2012; Rosdahl & Blaizot 2012), Re is expected to be very large at $Re \gtrsim 10^9$ (Andrey Kravtsov, private communication). In contrast to the laminar flows commonly shown in numerical simulations, the cold streams should be turbulent. Consequently, some fraction of the kinetic energy is expected to be converted into internal energy resulting in a more chaotic state of the flows, particularly in lower density part of the streams.

Empirically, the amount of turbulence in a gas can be determined from comparing the observed absorption line widths of two different atoms, because the line width is characterized by the Doppler parameter b which combines the effect of thermal broadening and bulk motion. Here we cannot use this approach to constrain the turbulent motion with only Mg II lines available and no additional information on the gas temperature. But in principle, we can estimate the degree of turbulent motion based on the observed velocity dispersion between different absorption components along different sightlines (e.g. Rauch et al. 2002).

On the other hand, the velocity dispersion observed along individual sightlines should indicate a combined effect of small-scale (~ 10 kpc) turbulent motion and large-scale (~ 100 kpc) gravitational acceleration. The comparable scale between the expected $v_{\rm circ}$ and observed $\delta\,v_{90}$ has led us to attribute the observed velocity dispersion along individual sightlines largely to gravitational acceleration, which implies a significantly smaller effect of turbulent motion on the observed line-of-sight velocity dispersion.

To obtain a crude estimate for the amount of turbulence in the infalling streams, we instead compare the difference in the optical depth weighted mean velocity ($\Delta\,v_\tau$) between pairs of sightlines. We restrict the comparison to only pairs that occur at similar projected distances, because of the apparent coherence in the observed velocity gradient with increasing distance (e.g. from B and C at $\rho \approx 44$ kpc to A and D at $\rho \approx 54$ kpc around $G1$).

For $G1$, sightlines B and C at $\rho \approx 44$ kpc are separated by $d_{\rm BC} \approx 8$ kpc in projected distance and the difference in $\Delta\,v_\tau$ is $|\Delta\,v_\tau(B) - \Delta\,v_\tau(C)| = 14$ km s^{-1}. Similarly, sightlines A and D at $\rho \approx 54$ kpc are separated by $d_{\rm BC} \approx 10$ kpc and the difference in $\Delta\,v_\tau$ is $|\Delta\,v_\tau(A) - \Delta\,v_\tau(D)| = 22$ km s^{-1}. Together, we estimate the velocity dispersion on scales of $d_s \sim 10$ kpc as a result of turbulent motion is of order $v_{\rm disp} \sim \sqrt{3}\,\Delta\,v_\tau \approx 35$ km s^{-1} at $\rho \approx 50$ kpc (roughly 1/3 of the virial radius) from $G1$.

For $G2$, sightlines C' and D' occur at $\rho = 31$ kpc and are separated by $d_{\rm C'D'} \approx 6$ kpc in projected distance. The Mg II absorbers uncovered along the two sightlines exhibit distinct kinematic features with $\delta\,v_{90} = 280$ and 102 km s^{-1}for C' and D', respectively. The distinct absorption profiles on scales of ~ 6 kpc already signal the presence of strong turbulence. Even if considering only the blue component in C' (component 1 in Table 3) as originating in the same stream, the velocity difference would be $|\Delta\,v_c^1(C') - \Delta\,v_c^1(D')| = 22$ km s^{-1} on scales of $d_s \sim 6$ kpc at $\rho = 31$ kpc (roughly 1/6 of the virial radius) from $G2$.

In summary, the observed velocity offsets between different sightlines suggest that halo gas around $G1$ and $G2$ is turbulent. The amount of turbulence is characterized by a velocity dispersion of ~ 35 km s^{-1} on scales of $6 - 10$ kpc at $\approx 30 - 50$ kpc from the star-forming disk.

5.2.2 Mass flow rate

A particularly interesting quantity regarding gaseous streams in galactic halos is the mass flow rate, which can be compared with model predictions. *However, there are a number of caveats that make an accurate estimate of this quantity difficult. For example, the size and orientation of the streams are not known. In addition, the streams in our study here are revealed by the presence of Mg II absorption doublet. Both the ionization fraction and metallicity of the gas are required in order to infer the total mass contained in the Mg II absorbers.* As described in § 4.1, we assume an ionization fraction of $f_{\rm Mg^+} = 0.1$ based on a simple ionization model presented in Chen & Tinker (2008) and infer a chemical enrichment level of $f_Z = 0.1 - 0.4$ solar metallicity for the Mg II absorbers around $G1$ and $f_z \approx 0.06$ solar for the Mg II absorbers around $G2$ based on the empirical metallicity–$W_r(2796)$ relation of Murphy et al. (2007).

The mass flow rate of streams probed by Mg II absorbers is characterized by the product of Mg II column density and cross section of the streams following,

$$\begin{aligned}\dot{M} &\equiv \frac{\Delta\,M}{\Delta\,t} = \frac{1}{f_{\rm Mg^+}}\frac{1}{f_Z}\left(\frac{\rm Mg}{\rm H}\right)_\odot^{-1}\frac{m_{\rm Mg}\,N({\rm Mg\,II})\,A_s\,(\cos\,i')\,v_s}{d\,\ell} \\ &= \frac{1}{f_{\rm Mg^+}}\frac{1}{f_Z}\left(\frac{\rm Mg}{\rm H}\right)_\odot^{-1}\frac{m_{\rm Mg}\,N({\rm Mg\,II})\,A_s\,v_{\rm los}}{d\,\ell}, \qquad (7)\end{aligned}$$

where $m_{\rm Mg}$ is the atomic weight of magnesium, $A_s \equiv \pi\, d_s^2/4$ is the cross section of the streams, i' is the orientation of infalling streams relative to the line of sight, v_s is the velocity of the streams, and $d\ell$ is the characteristic length of the streams probed by the sightline. Adopting a characteristic size of streams $d\ell \sim d_s$, we can approximate the mass flow rate as

$$\dot{M} \sim \frac{\pi}{4}\frac{1}{f_{\rm Mg^+}}\frac{1}{f_Z}\left(\frac{\rm Mg}{\rm H}\right)^{-1} m_{\rm Mg}\, N({\rm Mg\,II})\, d_s\, v_{\rm los} \quad (8)$$

$$\approx 4\times\frac{0.1}{f_{\rm Mg^+}}\frac{0.1}{f_Z}\frac{N({\rm Mg\,II})}{10^{13}{\rm cm^{-2}}}\frac{d_s}{10\,{\rm kpc}}\frac{v_{\rm los}}{100\,{\rm km/s}}\frac{\rm M_\odot}{\rm yr}. \quad (9)$$

For an observed line-of-sight velocity of $v_{\rm los} \approx 50$ km s^{-1} and a characteristic dimension of $d_s = 10$ kpc for the infalling streams probed by the Mg II absorbers, the inferred mass flow rate is $\dot{M} \sim 2\,{\rm M_\odot\,yr^{-1}}$.

6 SUMMARY

In conclusion, we have established spatially resolved velocity maps on scales of $5-10$ kpc for two galaxies at $z = 0.4-0.8$ using absorption spectroscopy of quadruply-lensed QSO HE 0435−1223 at $\rho \lesssim 50$ kpc from the galaxies. The analysis presented here demonstrates that multiple-QSO probes enable studies of spatially resolved gas kinematics around distant galaxies, which provide key insights into the physical nature of circumgalactic gas beyond the nearby universe. The main results of our study are summarized as the following:

(1) The first galaxy $G1$ at $z = 0.4188$ and $\rho \approx 50$ kpc from the quad-lens is best characterized as a typical, star-forming L_* galaxy with an on-going star formation rate of SFR $\sim 4\,{\rm M_\odot\,yr^{-1}}$ and total stellar mass of $M_* \approx (2-3)\times 10^{10}\,{\rm M_\odot}$. A strong Mg II absorber of $W_r(2796) > 1$ Å is detected in everyone of the four lensed QSO sightlines in the vicinity of the galaxy, indicating a high gas covering fraction and suggesting a chemical enricment level of $0.1-0.4$ solar in the halo gas. The Mg II absorption doublet is generallly characterized by a dominant component near the systemic velocity, which is followed by secondary absorbing components at ~ 100 km s^{-1} in the red. Such asymmetric kinematic signatures apply to all four sightlines separated by $8-10$ kpc in projected distances, and only a relatively small velocity shear (between $\Delta\, v \approx 20$ km s^{-1}) is seen across these different sightlines. The absorption profiles exhibit a strong spatial coherence on scales of ~ 10 kpc, suggesting the presence of bulk flows in the halos.

(2) The second galaxy $G2$ at $z = 0.7818$ and $\rho \approx 30$ kpc from the quad-lens is best characterized as a massive, super-L_* galaxy that resembles quiescent star-forming galaxies at $z = 0.5-1$. A moderately strong Mg II absorber of $W_r(2796) = 0.5-0.7$ Å is detected in everyone of the three lensed QSO sightlines observed in the vicinity of the galaxy, also indicating a high gas covering fraction and suggesting a chemical enricment level of ≈ 0.06 solar in the halo gas. While the Mg II absorption doublet around $G2$ also exhibit an asymmetric profile, distinct kinematic signatures are observed between different sightlines separated by ~ 6 kpc, suggesting a more turbulent nature of the halo gas.

(3) Interpreting the observed velocity shear around either $G1$ or $G2$ as a result of an underlying rotating gaseous disk leads to a velocity gradient as steep as $\partial\, v/\partial\, R = 16\pm 4$ km s^{-1} per kpc at $R > 55$ kpc, which is not seen in any nearby galaxies. We therefore conclude that the gas kinematics revealed by the MgII absorption around either G1 or G2 is inconsistent with expectations of a rotating disk.

(4) Interpreting the observed line-of-sight velocity shear across all four sightlines near $G1$ as a result collimated outflows would imply an increasing degree of collimation in the outflows with increasing distance. In addition, the inferred outflow speed is comparable to expectations from cosmic-ray driven winds, but is significantly smaller than expectations from accelerated outflows. While a single collimated outflows model cannot fully explain the spatially resolved gas kinematics around $G1$, it is conceivable that some fraction of the observed absorption components originate in collimated outflows. However, the inferred metallicity of the Mg II gas appears too low, in comparison to a solar metallicity (or higher) expected for the ISM gas of massive galaxies. In contrast, the inferred velocity gradient for $G2$ would substantially exceed model expectations. It is therefore unlikely that collimated outflows can explain the spatially resolved gas kinematics around $G2$.

(5) The strong spatial coherence in Mg II absorption across multiple sightlines is best explained by gaseous streams of $\gtrsim 10$ kpc in width driven by gravitational forces in the halo, either due to accretion from the IGM or stripped gas from interacting galaxies. This is supported for $G1$ by the presence of a nearby companion at 120 kpc away and by the low metal content inferred from the absorber strength. The absorption kinematics between sightlines at similar projected distances to the star-forming disk exhibit a velocity offset of ≈ 20 km s^{-1}. Interpreting the velocity difference as a result of turbulent motion leads to an estimate for the amount of turbulence in halo gas of ~ 35 km s^{-1} in velocity dispersion on scales of $6-10$ kpc at $\approx 30-50$ kpc from the star-forming disk.

ACKNOWLEDGMENTS

It is a pleasure to thank Denis Erkal, Nick Gnedin, Andrey Kravtsov, Lynn Matthews, and Michael Rauch for helpful discussions. We thank Chris Kochanek for providing the best-fit parameters of their lens model. We also thank the staff of the Las Campanas Observatory for their expert assistance with the observations. JRG gratefully acknowledges the financial support of a Millikan Fellowship provided by Caltech. KS acknowledges support from the University of Michigan's President's Postdoctoral Fellowship.

REFERENCES

Behroozi, P. S., Conrory, C., & Wechsler, R. H. 2010, ApJ, 717, 379

Bell, E. F., McIntosh, D. H., Katz, N., & Weinberg, M. D. 2003, ApJS, 149, 289

Bernstein, R. et al. 2003, Proc. SPIE, 4841, 1694, Shectman, S. A., Gunnels, S. M., Mochnacki, S., & Athey, A. E. 2003, Proc. SPIE, 4841, 1694

Birnboim, Y. & Dekel, A. 2003, MNRAS, 345, 349

Bland-Hawthorn J., Veilleux S., & Cecil G., 2007, Ap&SS, 311, 87
Boksenberg, A. & Sargent, W. L. W. 1978, ApJ, 220, 42
Boksenberg, A., Danziger, I. J., Fosbury, R. A. E., & Goss, W. M, 1980, 242, L145
Bond N. A., Churchill C. W., Charlton J. C., & Vogt S. S. ApJ 2001, 562, 641.
Booth, C. M., Agertz, O., Kravtsov, A. V., & Gnedin, N. Y. 2013, ApJL submitted (arXiv:1308.4974)
Bordoloi, R., Lilly, S. J., & Knobel, C. et al. 2011, ApJ, 743, 10
Bordoloi, R., Lilly, S. J., & Hardmeier, E. et al. 2013, ApJ submitted (arXiv: 1307.6553)
Bouché, N., Murphy, M. T., Péroux, C., Csabai, I., & Wild, V. 2006, MNRAS, 371, 495
Bouché, N., Hohensee, W., Vargas, R., Kacprzak, G. G., Martin, C. L., Cooke, J., Churchill, C. W. 2012, MNRAS, 426, 801
Bouché, N., Murphy, M. T., Kacprzak, G. G., Péroux, C., & Contini, T. 2013, Science, 341, 50 C. L. Martin,5 M. Dessauges-Zavadsky6
Chelouche, D. & Bowen, D. V. 2010, ApJ, 722, 1821
Chen, H.-W., Kennicutt, R. C., Jr., & Rauch, M. 2005, ApJ, 620, 703
Chen, H.-W. & Tinker, J. L. 2008, ApJ, 687, 745
Chen, H.-W., Helsby, J. E., Gauthier, J.R., Shectman, S. A., Thompson, I.B., & Tinker, J. L. 2010a, ApJ, 714,1521
Chen, H.-W., Wild, V., Tinker, J. L., Gauthier, J.-R., Helsby, J. E., Shectman, S. A., & Thompson, I. B. 2010b, ApJ, 724, L176
Chen, H.-W. 2012, MNRAS, 427, 1238
Chynoweth, K. M., Langston, G. I., Yun, M. S., Lockman, F. J., Rubin, K. H. R., & Scoles, S. A. 2008, ApJ, 135, 1983
Dekel, A. & Birnboim, Y. 2006, MNRAS, 368, 2
Dekel, A., Birnboim, Y., Engel, G., Freundlich, J., Goerdt, T., Mumcuoglu, M., Neistein, E., Pichon, C., Teyessier, R., & Zinger, E. 2009, Nature, 457, 451
Faber, S. M., Willmer, C. N. A., Wolf, C. et al. 2007, ApJ, 665, 265
Faucher-Giguère, C.-A. & Kereš, D. 2011, MNRAS, 412, L118
Fumagalli, M., Prochaska, J. X., Kasen, D., Dekel, A., Ceverino, D., & Primack, J. R. 2011, 418, 1796
Gauthier, J.-R. & Chen, H.-W. 2012, MNRAS, 424, 1952
Hanuschik, R. W. 2003, A&A, 407, 1157
Heckman, T. M., Armus, L., & Miley, G. K. 1990, ApJS, 74, 833
Heckman T. M., Lehnert M. D., Strickland D. K., & Armus L., 2000, ApJS, 129, 493
Heckman, T. M. 2002, Extragalactic Gas at Low Redshift (ASP Conf. Ser. 254), ed. J. S. Mulchaey & J. T. Stocke (San Francisco, CA: ASP), 292
Heiles, C. 1979, ApJ, 229, 533
Hunter, D. A., Wilcots, E. M., van Woerden, H., Gallagher, J. S., & Kohle, S. 1998, ApJ, 495, L47
Kacprzak, G. G., Churchill, C. W., Barton, E. J., & Cooke, J. 2011, ApJ, 733, 105
Kacprzak, G. G., Churchill, C. W., & Nielsen, N. M. 2012, ApJ, 760, L7
Kennicutt, R. C. Jr. & Evans, N. J. 2012, ARA&A, 50, 531
Kereš, D., Katz, N., Weinberg, D. H., & Davé, R. 2005, MNRAS, 363, 2
Kereš, D. Katz, N., Fardal, M., Davé, R., & Weinberg, D. H. 2009, MNRAS, 395, 160
Koorneef, J. et al. 1986, in Highlights of Astronomy (IAU), Vol.7, ed. J.-P. Swings, 833
Kornei, K. A., Shapley, A. E., Martin, C. L., Coil, A. L., Lotz, J. M., Schiminovich, D., Bundy, K., & Noeske, K. G. 2012, ApJ, 758, 135
Lanzetta, K. M., Bowen, D. V., Tytler, D., & Webb, J. K. 1995, ApJ, 442, 538
Ledoux, C., Petitjean, P., Fynbo, J. P. U., Møller, P., & Srianand, R. 2006, A&A, 457, 71
Lelli, F., Fraternali, F., & Sancisi, R. 2010, A&A, 516, A11
Lin, D. N. C. & Faber, S. M. 1983, ApJ, 266, L21
Marshall, J. L. et al. 2008, Proc. SPIE, 7014, 169
Martin C. L. & Bouché N., 2009, ApJ, 703, 1394
Martin, C. L., Scannapieco, E., & Ellison, S. L. et al. 2010, ApJ, 721, 174
Martin, C. L., Shapley, A. E., Coil, A. L., Kornei, K. A., Norman, N., & Pancoast, A. 2013, ApJ, 770, 41
Ménard B., Wild V., Nestor D., Quider A., Zibetti S., Rao S., & Turnshek D. 2011, MNRAS, 417, 801
Mihos, J. C., Keating, K. M., Holley-Bockelmann, K., Pisano, D. J., & Kassim, N. E. 2012, ApJ, 761, 186
Morgan, N. D., Kochanek, C. S., Pevunova, O., & Schechter, P. L. 2005, AJ, 129, 2531
Murphy, M. T., Curran, S. J., Webb, J. K., Ménager, J., & Zych, B. J. 2007, MNRAS, 376, 673
Murray N., Ménard B., & Thompson T. A., 2011, ApJ, 735, 66
Nestor, D. B., Johnson, B. D., & Wild, V. et al. 2011, MNRAS, 412, 1559
Noeske, K. G., Weiner, B. J., & Faber, S. F. et al. 2007, ApJ, 660, L43
Oppenheimer, B. D., Davé, R., Kereš, D., Fardal, M., Katz, N., Kollmeier, J. A., & Weinberg, D. H. 2010, MNRAS, 406, 2325
Pettini, M. & Pagel, B.E.J. 2004, MNRAS, 348, L59
Poggianti, B. M., Aragón-Salamanca, A., Zaritsky, D. et al. 2009, ApJ, 693, 112
Putman, M. E., Gibson, B. K., & Staveley-Smith, L. et al. 1998, Nature, 394, 752
Rauch, M., Sargent, W. L. W., & Barlow, T. A. 1999, ApJ, 515, 500
Rauch, M., Sargent, W. L. W., & Barlow, T. A. 2001a, ApJ, 554, 823
Rauch, M., Sargent, W. L. W., Barlow, T. A., Carswell, R. F. 2001b, ApJ, 554, 823
Rauch, M., Sargent, W. L. W., Barlow, T. A., Simcoe, R. A. 2002, ApJ, 576, 45
Rauch, M., Becker, G. D., Haehnelt, M. G., Gauthier, Jean-René, Ravindranath, S., & Sargent, W. L. W. 2011, MNRAS, 418, 1115
Rosdahl, J. & Blaizot, J. 2012, MNRAS, 423, 344
Rubin, K. H. R., Weiner, B. J., Koo, D. C., Martin, C. L., Prochaska, J. X., Coil, A. L., & Newman, J. A. 2010, ApJ, 719, 1503
Rubin, K. H. R., Prochaska, J. X., Ménard, B., Murray, N., Kasen, D., Koo, D. C., & Phillips, A. C. 2011, ApJ, 728, 55
Rubin, K. H. R., Prochaska, J. X., Koo, D. C., & Phillips, A. C. 2012, ApJ, 747, L26

Savaglio, S., Glazebrook, K., Le Borgne, D. et al. 2005, ApJ, 635, 260
Sofue, Y. & Rubin, V. 2001, ARA&A, 39, 137
Steidel, C.C., Kollmeier, J.A., Shapely, A.E., Churchill, C.W., Dickinson, M., & Pettini, M. 2002, ApJ, 570, 526
Steidel, C. C., Erb, D. K., Shapley, A. E., Pettini, M., Reddy, N., Bogosavljević, M., Rudie, G. C., & Rakic, O. 2010, ApJ, 717, 289
van de Voort, F. & Schaye, J. 2012, MNRAS, 423, 2991
Verheijen, M., van Gorkom, J. H., Szomoru, A., Dwarakanath, K. S., Poggianti, B. M., & Schiminovich, D. 2007, ApJ, 668, L9
Weiner, B. J. et al. 2009, ApJ, 692, 187
Werk, J. K. Prochaska, J. X., Thom, C., Tumlinson, J., Tripp, T. M., O'Meara, J. M., & Peeples, M. S. 2013, ApJS, 204, 17
White, S. D. M. & Rees, M. J. 1978, MNRAS, 183, 341
Wisotzki, L., Schechter, P. L., Bradt, H. V., Heinmüller, J., & Reimers, D. 2002, A&A, 395, 17
Wisotzki, L., Becker, T., Christensen, L., Helms, A., Jahnke, K., Kelz, A., Roth, M. M., & Sanchez, S. F. 2003, A&A, 408, 455
Wuyts, S., Frster Schreiber, N. M., & van der Wel, A. et al. 2011b, ApJ, 742, 96
Yun, M. S., Ho, P, T. P., & Lo, K. Y. 1994, Nature, 372, 530
Zhu, G., Blanton, M. R., & Burles, S.et al. 2011, ApJ, 726, 110